The Astrophysical Journal, 889:65 (16pp), 2020 January 20 https://doi.org/10.3847/1538-4357/ab621f

Continuum Enhancements, Line Profiles, and Magnetic Field Evolution during Consecutive Flares

Francesca Zuccarello[1], Salvo L. Guglielmino[1], Vincenzo Capparelli[1], Mihalis Mathioudakis[2], Peter H. Keys[2], Serena Criscuoli[3], Mariachiara Falco[4], and Mariarita Murabito[1,5]
[1] Dipartimento di Fisica e Astronomia "Ettore Majorana"—Sezione Astrofisica, Università degli Studi di Catania, Via S. Sofia 78, I-95123 Catania, Italy
salvatore.guglielmino@inaf.it
[2] Astrophysics Research Centre, School of Mathematics & Physics, Queen's University Belfast, Belfast, BT7 1NN, UK
[3] NSO—National Solar Observatory, Sacramento Peak—Box 62, Sunspot, NM 88349, USA
[4] INAF—Osservatorio Astrofisico di Catania, Via S. Sofia 78, I-95123 Catania, Italy
Received 2019 August 6; revised 2019 November 28; accepted 2019 November 29; published 2020 January 27

Abstract

During solar flares, magnetic energy can be converted into electromagnetic radiation from radio waves to γ-rays. Enhancements in the continuum at visible wavelengths, as well as continuum enhancements in the FUV and NUV passbands, give rise to white-light flares. In addition, the strong energy release in these events can lead to the rearrangement of the magnetic field at the photospheric level, causing morphological changes in large and stable magnetic structures like sunspots. In this context, we describe observations acquired by satellite instruments (*Interface Region Imaging Spectrograph* (*IRIS*), *Solar Dynamics Observatory*/Helioseismic and Magnetic Imager, *Hinode*/Solar Optical Telescope) and ground-based telescopes (Rapid Oscillations in the Solar Atmosphere (ROSA)/Dunn Solar Telescope) during two consecutive C7.0 and X1.6 flares that occurred in active region NOAA 12205 on 2014 November 7. The flare was accompanied by an eruption. The results of the analysis show the presence of continuum enhancements during the evolution of the events, observed both in ROSA images and in *IRIS* spectra. In the latter, a prominent blueshifted component is observed at the onset of the eruption. We investigate the role played by the evolution of the δ sunspots of the active region in the flare triggering, and finally we discuss the changes in the penumbrae surrounding these sunspots as a further consequence of these flares.

Unified Astronomy Thesaurus concepts: Solar flares (1496); Solar white-light flares (1983); Solar magnetic reconnection (1504); Active solar chromosphere (1980); Solar chromosphere (1479); Solar photosphere (1518); Solar transition region (1532); Solar ultraviolet emission (1533); Solar magnetic fields (1503); High resolution spectroscopy (2096)

Supporting material: animations

1. Introduction

Solar flares are complex eruptive phenomena occurring in the atmospheric layers of the Sun, releasing energy spanning typically from 10^{28} to 10^{32} erg. They are often triggered by the destabilization of a filament located above a polarity inversion line (PIL; see, e.g., Fletcher et al. 2011 for a review and references therein). This energy, previously stored in a nonpotential magnetic field configuration, is converted, through magnetic reconnection, in kinetic energy, bulk plasma motions, and electromagnetic radiation emitted through the whole spectrum, from decameter radio waves to gamma-rays at 100 MeV (see, e.g., Benz 2017). Far-reaching consequences may be due to such strong energy release phenomena, with potential impact on Earth (Zuccarello et al. 2013; Patsourakos et al. 2016; Piersanti et al. 2017).

Most of the flare emission signatures observed at different wavelengths can be explained in the framework of the CSHKP two-dimensional (2D) magnetic reconnection model, named for Carmichael (1964), Sturrock (1966), Hirayama (1974), and Kopp & Pneuman (1976): in a coronal arcade, a magnetic reconnection process caused, for instance, by the eruption of a filament takes place, so that the field lines of the arcade confining the flux rope get opened and later reconnect. At the increasing reconnection heights that characterize the arcade field lines, from the innermost to the outermost, electrons and protons are accelerated and, when colliding with the lower atmospheric layers, can impulsively heat the local plasma (Fletcher & Hudson 2008) and cause the chromospheric evaporation which fills the postflare loops (Milligan 2015).

A more realistic three-dimensional (3D) treatment of magnetic reconnection allows the interpretation of some of the flare properties that cannot be understood in the framework of the CSHKP model, such as the evolution of the shear of flare loops, their morphology and relative positioning, and the motions of EUV or X-ray sources along the ribbons (e.g., Aulanier et al. 2012, 2013; Janvier et al. 2013; more recently, Janvier 2017). Three-dimensional reconnection occurs in the quasi-separatrix layers (e.g., Démoulin 2006 and references therein), where the displacement of the magnetic field lines determines a continuous exchange of connectivities with the neighboring field lines. In the lower atmosphere, this process appears as an apparent slipping motion of the field-line footpoints, which correspond to the flare ribbons and is referred to as *slipping reconnection* (Aulanier et al. 2006, 2007). This 3D solar flare model has been verified in many observations (Dudík et al. 2014, 2016; Sobotka et al. 2016; Zheng et al. 2016). In particular, such complex dynamics seem to be favored when flares occur in active regions (ARs) with intricate

[5] Currently at INAF—Osservatorio Astronomico di Roma, via Frascati 33, I-00078 Monte Porzio Catone, Italy.

magnetic configurations, like those hosting δ sunspots, where a fan-spine topology is usually formed (e.g., Guglielmino et al. 2016).

In the visible range, the emission is commonly observed in the Hα line and is believed to be due to the effect of collisions on the chromospheric plasma by the energetic particles accelerated at the reconnection site and precipitating toward lower heights. This emission, which already displays an increase during the impulsive phase, is often observed in the form of two bright ribbons, located parallel to the PIL and separating from each other with an initial velocity of $\sim$100 km s^{-1}, decreasing to less than 1 km s^{-1} in the following tens of minutes to hours (see, e.g., Maurya & Ambastha 2009). Indeed, taking into account the 3D nature of magnetic reconnection, in the presence of a fan-spine topology, flares may exhibit extra ribbons or even circular ribbons (Masson et al. 2009; Romano et al. 2017).

Observations show that increased emission is also detected in the visible continuum, i.e., in white light (WL), and is often spatially and temporally correlated with hard X-ray (HXR; $\sim$10 keV) signatures (see, e.g., Hudson et al. 1992). In this regard, we recall that WL flares were initially believed to be associated only with large X-class events, that is, when the EUV or soft X-ray emission could exceed a certain threshold (Neidig & Cliver 1983). However, successive observations provided evidence of the presence in the continuum of bright kernels of size $\approx$1″–3″, whose location was cospatial with the more extended flare ribbons detected in the core of strong lines, like the Hα and Ca II lines (Neidig 1989). More recently, Jess et al. (2008) have shown that WL emission can also be observed during C-class flares.

As a result of the rapid restructuring of the 3D magnetic field driven by magnetic reconnection, photospheric structures can be affected by flares. Sudden and irreversible changes of the photospheric magnetic field may occur in spite of the large inertia of the photosphere (see the reviews of Wang & Liu 2015; Toriumi & Wang 2019). In particular, also considering WL observations, it has been observed that penumbral structures usually decay in the peripheral sides of δ sunspots hosting flares, whereas they darken near the flaring PILs. Several recent observations demonstrated that the transverse field is enhanced at the central flaring PILs (e.g., Petrie & Sudol 2010; Petrie 2012, 2013; Wang et al. 2012a, 2012b, 2014). In general, most of the changes are localized around the PIL regions (Castellanos Durán et al. 2018; Lu et al. 2019).

In this framework, the main goal of this work is to investigate if and how continuum emission and changes in line profiles during flares are associated with rearrangements in the magnetic field. We study two consecutive flares that occurred in AR NOAA 12205 (hereafter, AR 12205) on 2014 November 7 using data acquired from ground-based and satellite instruments. The strongest flare, classified as an X1.6 event, was also analyzed by Yurchyshyn et al. (2015) using different data sets. We identify the complex configuration of AR 12205, comprising two δ sunspots, as the possible flare trigger. We study the characteristics of the emission both in UV spectral lines and in the continuum (UV and visible wavelengths) during the evolution of the events. We also correlate the observed continuum changes induced in the photospheric structures with the rearrangement of the magnetic field.

The paper is organized as follows: in Section 2 we describe the observational data. In Section 3, the data analysis and the results are reported. In Section 4, we discuss the results, describing our conclusions in Section 5.

2. Observations

AR 12205, located at N15E33 on 2014 November 7, was characterized by a $\beta\gamma\delta$ magnetic configuration and produced several flares with various X-ray classifications. In particular, on 2014 November 7, an M1.0 flare (peak at 10:13 UT) and a series of C-class flares (C3.9, peak at 12:03 UT; C1.3, 13:19 UT; C2.3, 13:55 UT; C7.0, 14:51 UT; C7.0, 16:10 UT) occurred before the onset of an X1.6 flare (peak at 17:26 UT).

We observed this AR during a coordinated observing campaign carried out using the ground-based Rapid Oscillations in the Solar Atmosphere (ROSA; Jess et al. 2010) imaging system mounted at the Dunn Solar Telescope at the US National Solar Observatory in New Mexico and the *Interface Region Imaging Spectrograph* (*IRIS*; De Pontieu et al. 2014) satellite (see Figures 1 and 2).

The ROSA data were acquired simultaneously in the Ca II K core at 3933.7 Å (bandpass 1.0 Å), in the blue continuum at 4170 Å (bandpass 52.0 Å), and in the *G* band at 4305.5 Å (bandpass 9.2 Å), in two different fields of view (FOVs): FOV1 was acquired between 15:38 and 16:31 UT, while FOV2 was acquired between 16:50 and 18:53 UT (see the solid-line squares in Figure 1 and the blue rectangles in Figure 2). The Ca II K, *G*-band, and continuum observations were obtained with a diffraction-limited spatial sampling of 0.″069 pixel^{-1}. The total FOV is 69″ × 69″. High-order adaptive optics were applied throughout the observations (Rimmele 2004). The images were then reconstructed by implementing the speckle algorithms of Wöger et al. (2008) followed by de-stretching. These algorithms removed the effects of atmospheric distortion from the data. The effective cadence after reconstruction is reduced to 2.3 s for Ca II K and 2.112 s for the *G* band and continuum. Moreover, during the speckle reconstruction, an apodization windowing function is applied to the images to reduce artifacts introduced by Fourier transforms. This process reduces the FOV of the images to 58.″65 × 58.″65 (see Figure 3).

IRIS acquired slit-jaw images (SJIs) in three passbands (C II at 1330 Å, Mg II k at 2796 Å, and Mg II wing at 2832 Å). The large four-step coarse raster mode was used for the slit, acquiring data from 16:07 to 16:57 UT and from 17:45 to 18:35 UT (see the green rectangles in the upper part of the plot shown in Figure 2). The SJI filtergrams (80 for each interval of acquisition) were characterized by an FOV of 119″ × 119″ with a sampling of 0.″166 pixel^{-1} and a temporal cadence of 37 s. The FOV of the raster was 6″ × 119″ with a sampling of 0.″166 pixel^{-1} and a temporal cadence of 37 s, with a step cadence of 9.4 s.

The analysis carried out in this study is based mainly on the Mg II k & h lines at 2796.35 Å and 2803.55 Å (characterized by a formation temperature of log T [K] = 4.0), as well as C II at 1330 Å and Si IV at 1403 Å (having formation temperatures of log T [K] = 4.3 and 4.8, respectively; De Pontieu et al. 2014). The central wavelength for each analyzed line has been determined by ensuring that the cool S I 1401.515 Å and Ni II 2799.474 Å lines were at rest within $\pm$5 km s^{-1} for the FUV and NUV channels, respectively.

Context images acquired by the Helioseismic and Magnetic Imager (HMI; Scherrer et al. 2012; Hoeksema et al. 2014) instrument on board the *Solar Dynamics Observatory* (*SDO*, Pesnell et al. 2012) satellite were used to obtain information on the global magnetic field configuration of AR 12205. More precisely, full-disk continuum images and longitudinal (line-of-

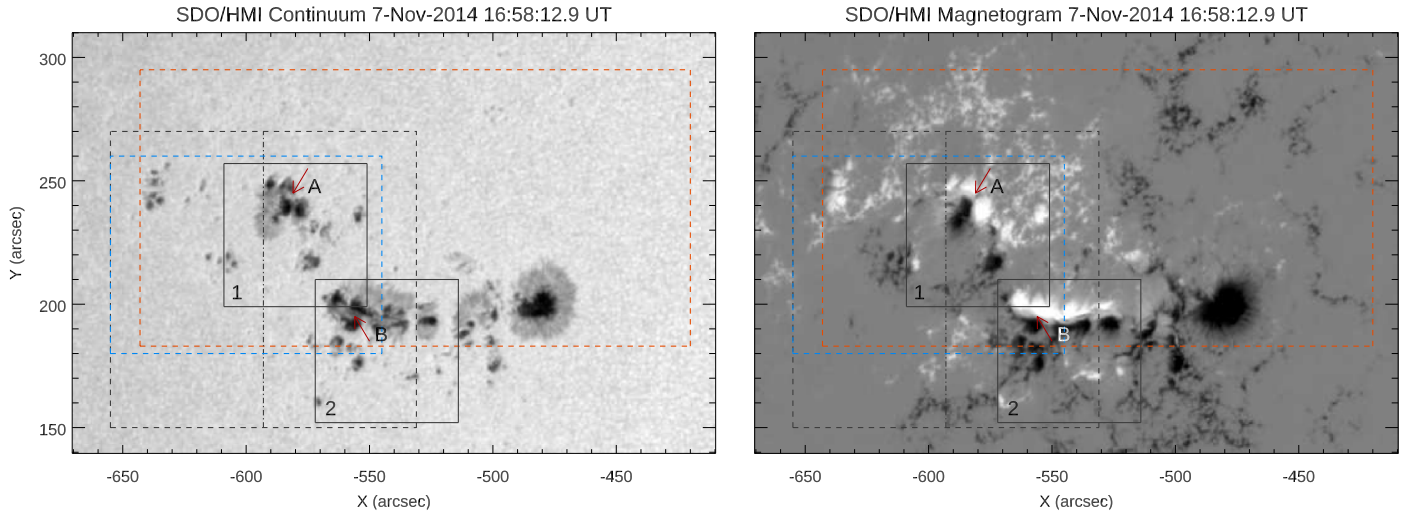

Figure 1. Left: *SDO*/HMI continuum intensity map showing the morphology of AR 12205 on 2014 November 7 at 16:58:12 UT. Right: *SDO*/HMI line-of-sight magnetogram showing the magnetic configuration of the AR at the same time. In both maps, the dashed black box indicates the *IRIS* SJI FOV and the dotted-dashed vertical line shows the approximate position of the slit during the *IRIS* raster observations; the dashed blue box indicates the *IRIS* SJI sub-FOV used in Figure 5. The two solid-line boxes indicate the FOVs acquired by the ROSA instrument at different times. Labels 1 and 2 in these boxes indicate FOV1 and FOV2, respectively (see main text). The red dashed box indicates the *Hinode*/SOT FOV. The red arrows in both maps indicate the presence of two δ spots, labeled with letters *A* and *B*, respectively. In these and in the following images, if not otherwise specified, north is to the top, and west is to the right.

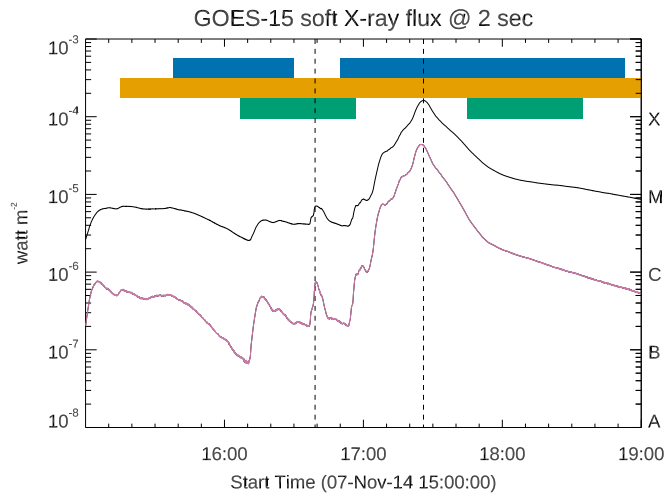

Figure 2. *GOES* soft X-rays in two wavelength ranges: 1.0–8.0 Å (black line) and 0.5–4 Å (magenta line) showing the flux increase during the flares analyzed in the paper. The peak time of the C7.0 (16:39 UT) and X1.6 (17:26 UT) flares is indicated by vertical dashed lines. The blue rectangles indicate the time intervals of acquisition of the ROSA instrument for FOV1 (left) and FOV2 (right). Analogously, the orange rectangle indicates the time interval of acquisition of the *Hinode*/SOT, and the green rectangles indicate the time intervals of acquisition of the *IRIS* instrument.

sight, LOS) magnetograms taken by HMI in the Fe I line at 6173 Å with a resolution of 1″ were used to complement the high-resolution data set of the ground-based instruments. In the present work, we also considered full-disk data from the Atmospheric Imaging Assembly (AIA; Lemen et al. 2012) on board the *SDO* satellite. We used images from the 1600, 304, 171, 335, and 131 Å channels. The cadence of the *SDO*/AIA data is 24 s for the UV channel and 12 s for the EUV channels, respectively, with a spatial scale of about 0.″6 pixel^{-1}. *SDO*/AIA images were also compensated for solar rotation effects.

We also benefit from high-resolution photospheric observations obtained with the Solar Optical Telescope (SOT; Tsuneta et al. 2008) aboard the *Hinode* satellite (Kosugi et al. 2007). A sequence of filtergrams in the *G* band (430.5 ± 0.8 nm) on AR 12205 was acquired between 15:15 UT and 19:06 UT on November 7, with an uneven cadence of about 10 minutes. A simultaneous sequence was acquired in the Ca II H line (396.85 ± 0.3 nm), with a cadence of 1 minute. These data cover an FOV of about 223″ × 111.″5.

3. Data Analysis

As previously stated, AR 12205 was characterized by a $\beta\gamma\delta$ configuration. In particular, from the comparison of the HMI continuum image shown in Figure 1 (left) with the HMI LOS magnetogram reported in Figure 1 (right), it is possible to infer that this active region hosted two δ spots. The first one, labeled with the letter *A* and indicated by the arrow pointing approximately at [−580″, 245″] in Figure 1, was characterized by the presence of penumbral filaments running almost parallel to the umbrae borders (see, e.g., Cristaldi et al. 2014), as shown in the ROSA *G*-band image reported in Figure 3 (top-right panel). The other δ spot, labeled with the letter *B* and located in the region indicated by the arrow pointing at [−560″, 190″] in Figure 1, was part of an area characterized by a magnetic neutral line running almost parallel to the equator. Also in this case, the δ spot is characterized by penumbral filaments running parallel to the opposite-polarity umbrae, as shown in the ROSA *G*-band image reported in Figure 3 (middle panels).

During the observing interval, two flares took place in AR 12205: a C7.0 class flare (`SOL2014-11-07T16:10`, start time 16:10 UT, peak 16:39 UT, end 16:45 UT), and an X1.6 class flare (`SOL2014-11-07T16:53`, start time 16:53 UT, peak 17:26 UT, end 18:34 UT). The dashed vertical lines in Figure 2 indicate the flare peaks.

From an inspection of Figure 1 (left), showing the photospheric configuration of AR 12205, it is possible to infer that the SJI FOV (dashed-line square) roughly includes both ROSA FOVs, although it should be stressed that the slit position allowed us to follow only the evolution of the northern part of the flares, where δ-complex *A* was located.

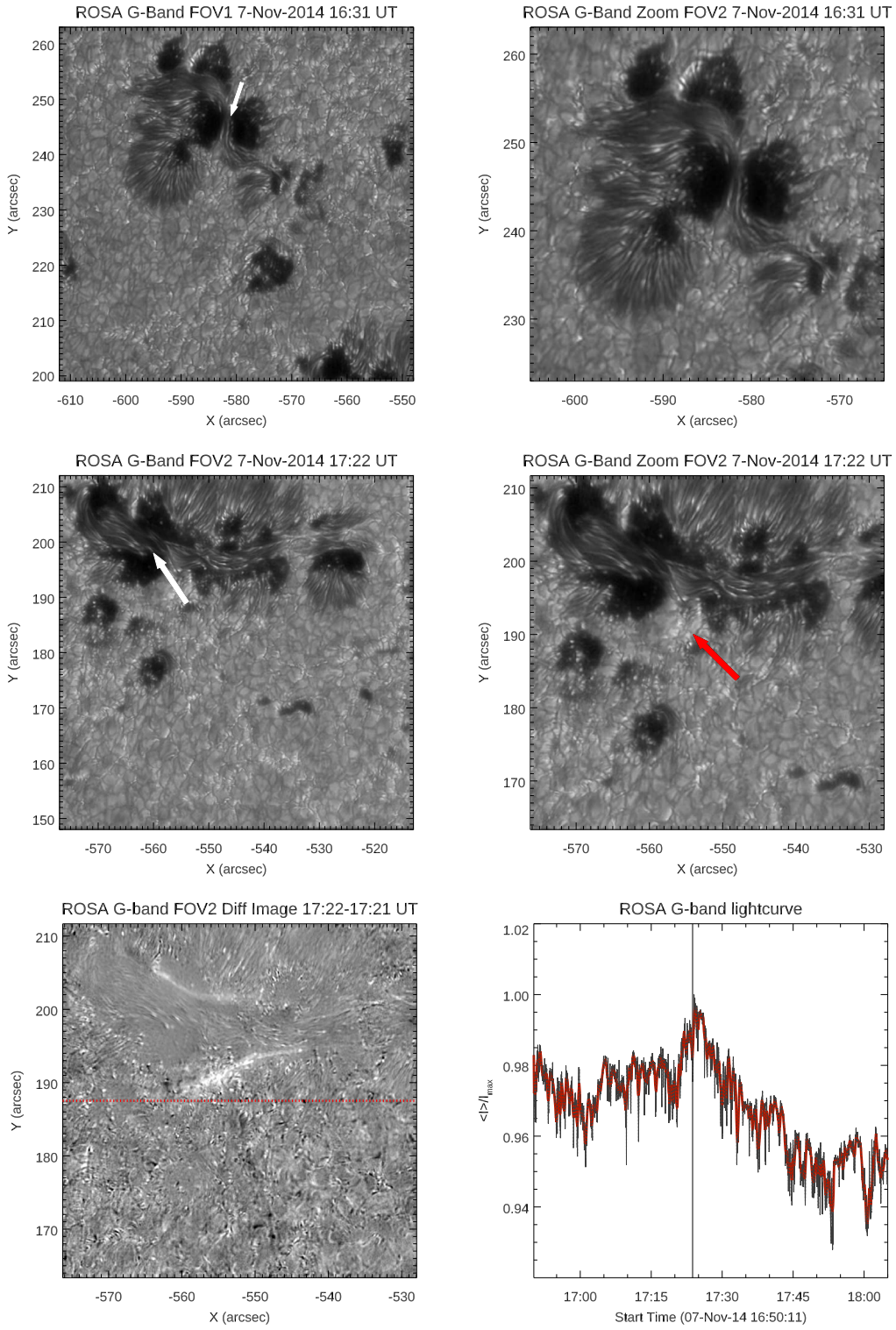

Figure 3. ROSA *G*-band images of AR 12205. Top panels: (left) the entire FOV1, at 16:31 UT. The white arrow indicates the δ-spot *A*. (Right) Zoomed image from ROSA FOV1 showing the details of δ-spot *A*, characterized by the presence of sheared penumbral filaments within the two opposite magnetic polarities. Middle panels: (left) the entire FOV2 at 17:22 UT, during the rise phase of the X1.6 flare, a few minutes before the peak. The white arrow indicates the δ-spot *B*. (Right) Zoomed image from ROSA FOV2 showing the location of a ribbon observed in the continuum (red arrow) at 17:22 UT. Bottom panels: (left) difference imaging of zoomed FOV2, showing the ribbons at a time close to the peak of the X1.6 flare. The red dotted line separates the zoomed FOV2 into two halves. (Right) *G*-band lightcurve relevant to the upper half of the zoomed FOV2, where the ribbons are observed. The red line represents a smoothed trend. The vertical line indicates the X1.6 flare peak. An animation of the *G*-band images relative to the zoomed FOV2 is available. The video begins at 16:50:11 UT and ends at 17:40:03 UT. The real-time duration is 43 s. Note the passage of the ribbon at around 17:22 UT.

(An animation of this figure is available.)

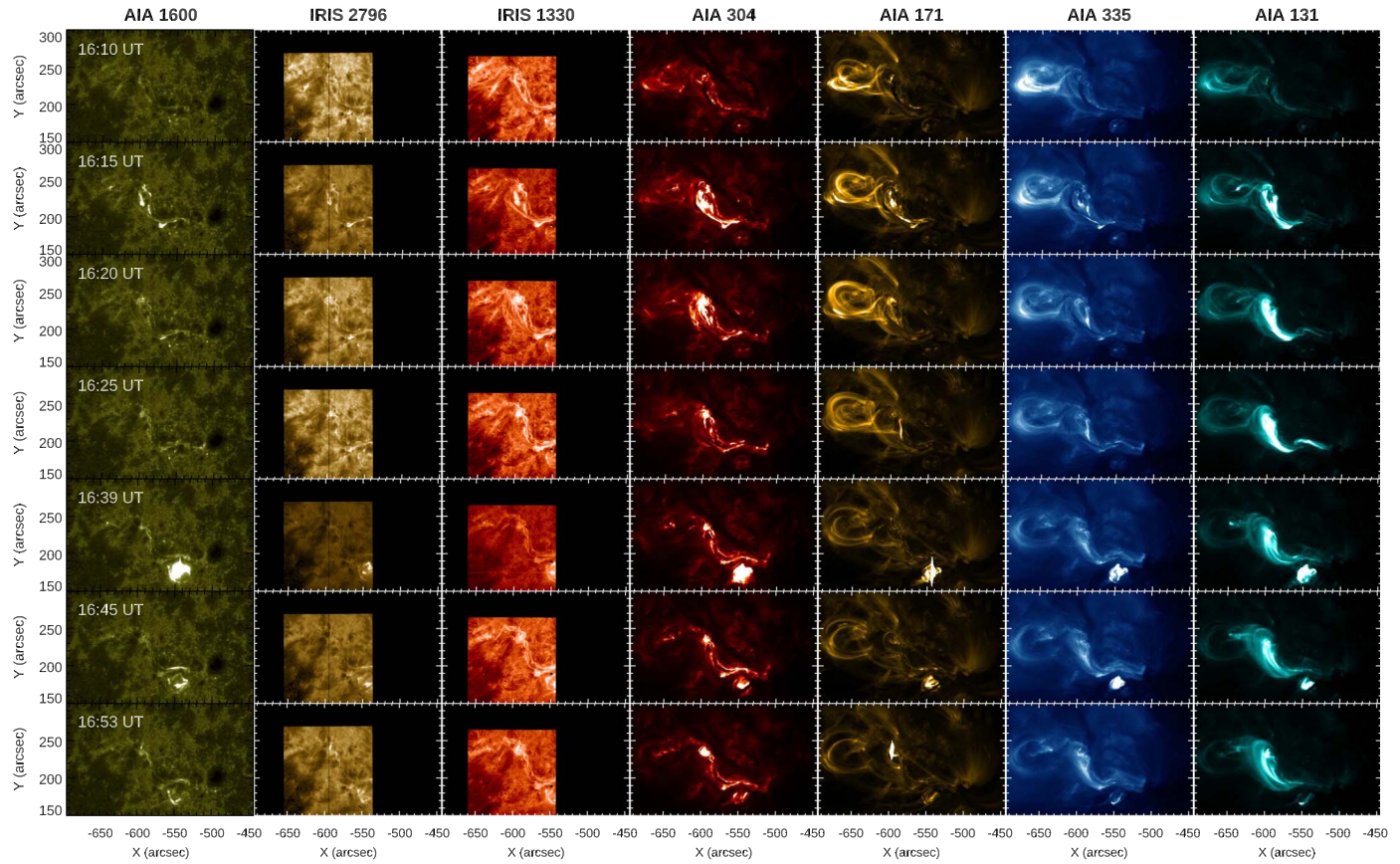

Figure 4. Synoptic view of the evolution of the C7.0 flare at different atmospheric layers, at representative times during the observing interval. From left to right, each row shows the *SDO*/AIA 1600 Å map, the *IRIS* SJI 2796 Å and 1330 Å maps, and the *SDO*/AIA cospatial maps for the selected EUV channels.

3.1. The C7.0 Flare Evolution

Figure 4 displays the evolution of the C7.0 flare at different atmospheric heights, from the upper photosphere (*SDO*/AIA 1600 Å) up to the hot corona (*SDO*/AIA 131 Å), including high-resolution observations by *IRIS* in the upper chromosphere (SJI 2796 Å) and transition region (SJI 1330 Å). The FOV analyzed here covers almost the same region as in Figure 1, having been slightly extended to accommodate coronal loops of AR 12205 within the images.

At the start time of the flare (16:10 UT), a prominent dark filament is seen in the coronal channels (304, 171, 335, and 131 Å) connecting δ-complex *A* and δ-complex *B*. While the filament is being lifted (16:15 UT), brightenings are seen from coronal levels down to the lower atmosphere (e.g., 1600 Å and 2796 Å) in both δ-complexes *A* and *B*. Some remote brightenings are also observed, for instance the one located at [−640″, 240″], which can be explained in terms of the connectivities of AR 12205 in the upper atmospheric layers (compare to the 131 Å image). Energy release, likely due to small-scale reconnection episodes in the region where magnetic field lines have been pushed into by the rising filament, causes intensity enhancements in this area at transition region heights (1330 Å and 304 Å). At 16:20 UT, there is an apparent motion of plasma toward δ-complex *A* and a null point seems to form (see at [−620″, 230″] in the 171 Å map). The dark filament is being shaken, but it is not launched off. The null point is still very visible at 16:25 UT ([−620″, 220″] in the 171 and 335 Å maps), while at the base of the dome-shaped domain under the null point, a bright patch at $X = (-580'')$, elongated along the *Y* direction, is seen in all channels, down to the chromosphere. In the full sequence, this bright patch is seen moving southward. At the peak, the C7.0 flare exhibits a circular ribbon, which occurs in the area of δ-complex *B*. The dark filament has settled down, acquiring a sigmoidal configuration along the PIL of the AR (see the 304 Å maps at 16:39 UT and 16:45 UT). Shortly after the C7.0 flare ends, the X1.6 flare starts (16:53 UT).

3.2. The X1.6 Flare Evolution

In the following, we will describe the evolution of the main X1.6 flare and several phenomena that can be recognized during its occurrence.

3.2.1. The Onset of the Flare

Figure 5 displays the maps obtained from the *IRIS* SJIs acquired in the three wavelengths: SJI 1330 Å (first panel), SJI 2796 Å (second panel), and SJI 2832 Å (third panel). The portion of the simultaneous *Hinode*/SOT Ca II H filtergram cospatial to the *IRIS* maps is also displayed (fourth panel). We indicate with boxes the subfields of the full FOV (sub-FOVs) used for the subsequent analysis.

In Figure 6 we plot a time sequence of the sub-FOVs indicated with a solid-line box in Figure 5 containing the northern δ-complex *A*, composed of SJIs at 1330 Å (first column) and 2796 Å (second column), and the nearly simultaneous cospatial *Hinode*/SOT Ca II H images (third column). The sequence, referring to the start time of the X1.6 flare (16:53 UT) and following instants, shows that the flare initiated between the two opposite-polarity umbrae of δ-sunspot *A*. Both *IRIS* and *Hinode*/

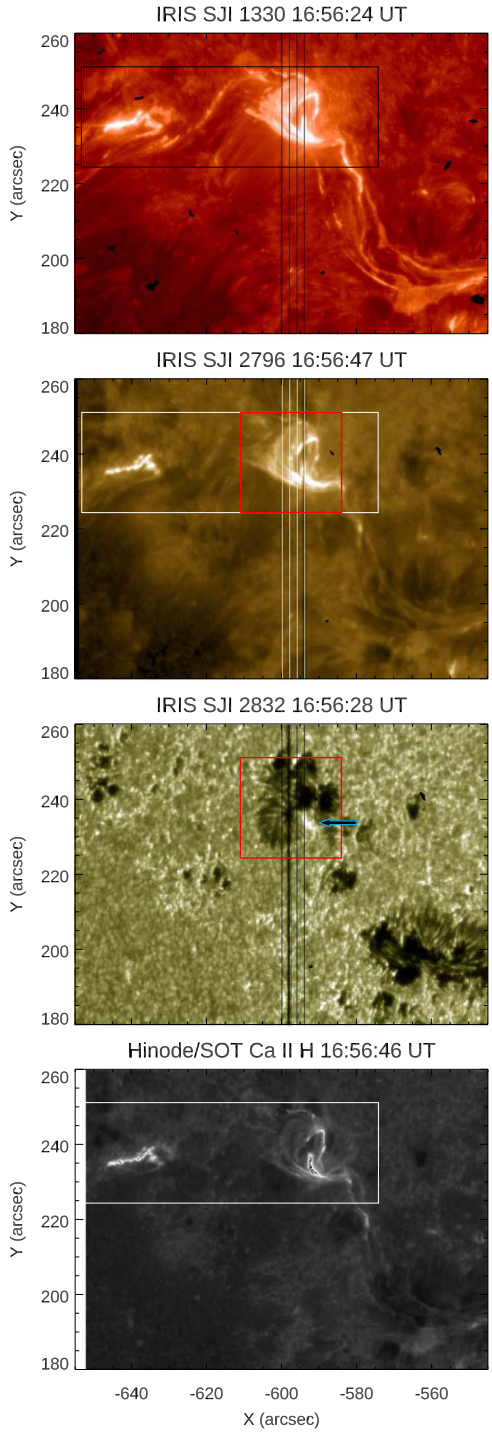

Figure 5. Top panels: maps derived from *IRIS* SJI images acquired on 2014 November 7 at around 16:56 UT, showing a portion of the FOV recorded by the instrument at three different wavelengths: SJI 1330 Å (first panel), SJI 2796 Å (second panel), and SJI 2832 Å (third panel). In each image, the dashed vertical lines indicate the raster positions during the acquisition time. Bottom panel: *Hinode*/SOT Ca II H filtergram simultaneous with *IRIS* SJI images. The solid-line box indicates the sub-FOV analyzed in Figure 6. The red-line box frames the sub-FOV zoomed in Figure 7. The arrow in the third panel indicates the brightening. An animation of the *Hinode*/SOT Ca II H images is available. The video begins at 16:51:47 UT and ends on 17:05:47 UT. The real-time duration is 5 s. The ejection of the flux rope is clearly visible.

(An animation of this figure is available.)

SOT observed the emergence and subsequent expansion of bright loops from the δ-sunspot. These formed an expanding flux rope, as indicated by the arrow in the Ca II H filtergram at 16:55 UT. Notably, at around 16:56 UT, this loop system broke up into two different branches. Yurchyshyn et al. (2015) observed the development of these structures also in *SDO*/AIA images. Also, we notice prior to the breaking of the bright loops, a third luminous elongated patch appears about 30″ to the east of the loop system visible in *IRIS* 1330 Å and 2796 Å, and even more evident in the Ca II H filtergrams. While *IRIS* observations abruptly end just a few moments after the breaking of the loop system and flux rope ejection, Ca II H images follow the subsequent evolution of the flare: the eastern elongated patch becomes stronger in intensity, growing in size and slightly moving. At 16:59 UT, the loop system is definitely broken apart and the two ribbons appear clearly. The evolution of the onset of the flare can also be seen in the movie for the *Hinode*/SOT Ca II H images related to Figure 5.

3.2.2. Enhancements in the Continuum and in Lines

At around 16:56 UT, that is, at the beginning of the rise phase of the X1.6 flare, the *IRIS* SJI image in the Mg II wing at 2832 Å shows an intensity enhancement in the site at $X = (-595'', -590'')$, $Y = (230'', 235'')$ in Figure 5 (third panel). This intensity enhancement has the shape of a small arch that moves toward the southeast direction, encountering therefore the place monitored by the *IRIS* slit (see also Figure 7, bottom panel). Unfortunately, the *IRIS* satellite after this time changed its target, so we do not have a complete coverage of the phenomena occurring during this flare. Nevertheless, it has been possible to study the intensity enhancement and the plasma motions at the time when the slit was on the flare ribbon.

At around 17:22 UT, i.e., a few minutes before the peak of the X1.6 flare, WL ribbons were detected close to the southern δ-spot *B* in both the *G* band and the 4170 Å continuum images acquired with ROSA (FOV2; see also the animation for Figure 3). In particular, the southernmost ribbon is clearly visible in the images obtained in these wavelength ranges, while the northern ribbon can only be distinguished using difference imaging (see, e.g., Figure 3, bottom-left panel). The ribbons separate with a velocity of $\approx$10 km s^{-1}. In Figure 3 (bottom-right panel), we plot the lightcurve obtained using the *G*-band sequence. It was calculated at the location of the flare ribbons, in the upper half of the zoomed FOV2 where the flare ribbons are located. It clearly illustrates that an intensity enhancement is found almost simultaneously with the flare peak.

In Figure 8, we display the radiometric calibrated intensities in five *IRIS* spectral windows expressed in physical units (erg cm^{-1} s^{-1} sr^{-1} per pixel), which have been obtained from the sub-FOV with the IRIS_CALIB_SPEC routine. Profiles shown in blue refer to the average intensity in the pixel at slit position (3; 538) with its adjacent pixels (3; 537) and (3; 539), relative to raster 79. The approximate position of these pixels is shown in Figure 7, with a blue circle; the other circles (orange and green) shown in the same Figure 7 refer to the other pixels studied in this work. The position indicated by the blue circle corresponds to [−593.″8, 232.″3] at 16:56:47 UT, at the beginning of the X1.6 flare. Analogously, profiles shown in

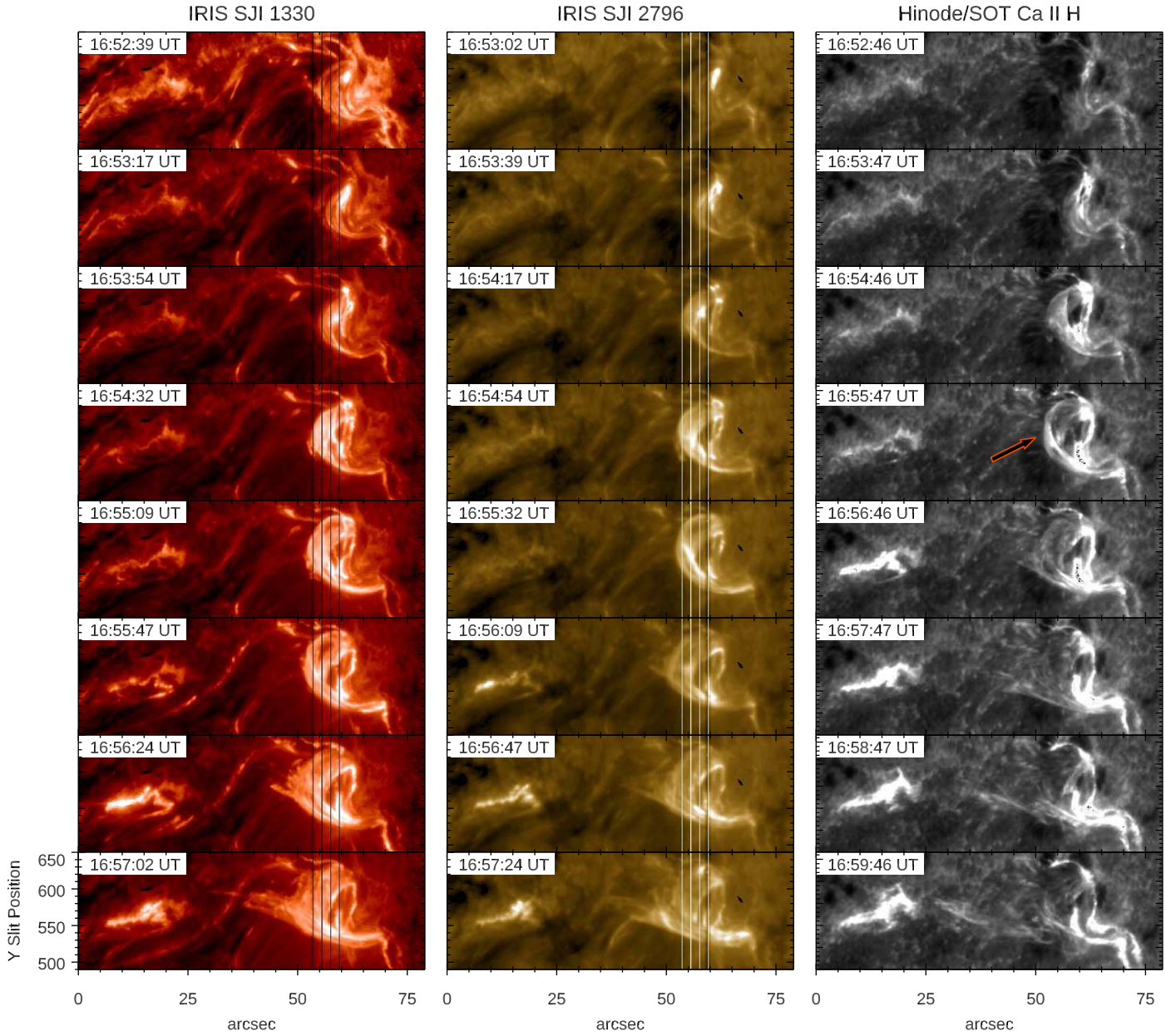

Figure 6. The evolution of the flaring site around the northern δ-spot *A* at the beginning of the X1.6 flare, on 2014 November 7, in three different wavelengths: *IRIS* SJI 1330 Å (left), *IRIS* SJI 2796 Å (middle), and *Hinode*/SOT Ca II H (right). In the *IRIS* SJIs, the dashed vertical lines indicate the raster positions during the acquisition time. The arrow in the Ca II H filtergram indicates the expanding flux rope, which is launched during the sequence.

orange refer to the average intensity in the pixel at slit position (3; 544) with its adjacent pixels (3; 543) and (3; 545) for the same raster. This position corresponds to [−593.″8, 233.″3]. Finally, profiles shown in green refer to the average intensity in the pixel at slit position (3; 559), with its adjacent pixels (3; 558) and (3; 560) for the same raster, the position corresponding to [−593.″8, 235.″8] solar coordinates. For comparison, in the same plot, the average intensity calculated at the same time along the slit at 20 consecutive pixel positions (from 160 to 179), in a quiet-Sun region, is shown with a black solid line.

It is evident that in all the channels there is an intensity enhancement also in the continuum region, with the exception being the 2832 Å spectral window. Nevertheless, in the latter we also see emission in the flaring pixel at (3; 559) corresponding to absorption features in the quiet Sun.

Interestingly, the blue pixel exhibits a very prominent bump in the blue wing of the Si IV 1402 Å line, as well as in the blue wings of C II 1334 and 1336, and the Mg II h and k lines. It is worth highlighting that this slit position corresponds to the apparent point where the loop systems studied in Figure 6 splits into two branches, as clearly seen in Figure 7 (top panel).

In Figure 9 we show a sample of the line profiles at different pixel positions of the *IRIS* slit, where the bright ribbon close to δ-spot *A* was observed.

The analysis of the Si IV 1402.8 Å profiles reported in Figure 9 (top panels) indicates that at the position of the green pixel, during the analyzed time interval there is a strong downflow with velocities reaching 100 km s^{-1}; the line is saturated at 16:55:32 and 16:56:09 UT. The profiles relative to the orange pixel show a sudden change from upflows (−90 km s^{-1}) to downflows (up to 80 km s^{-1}); the line shows

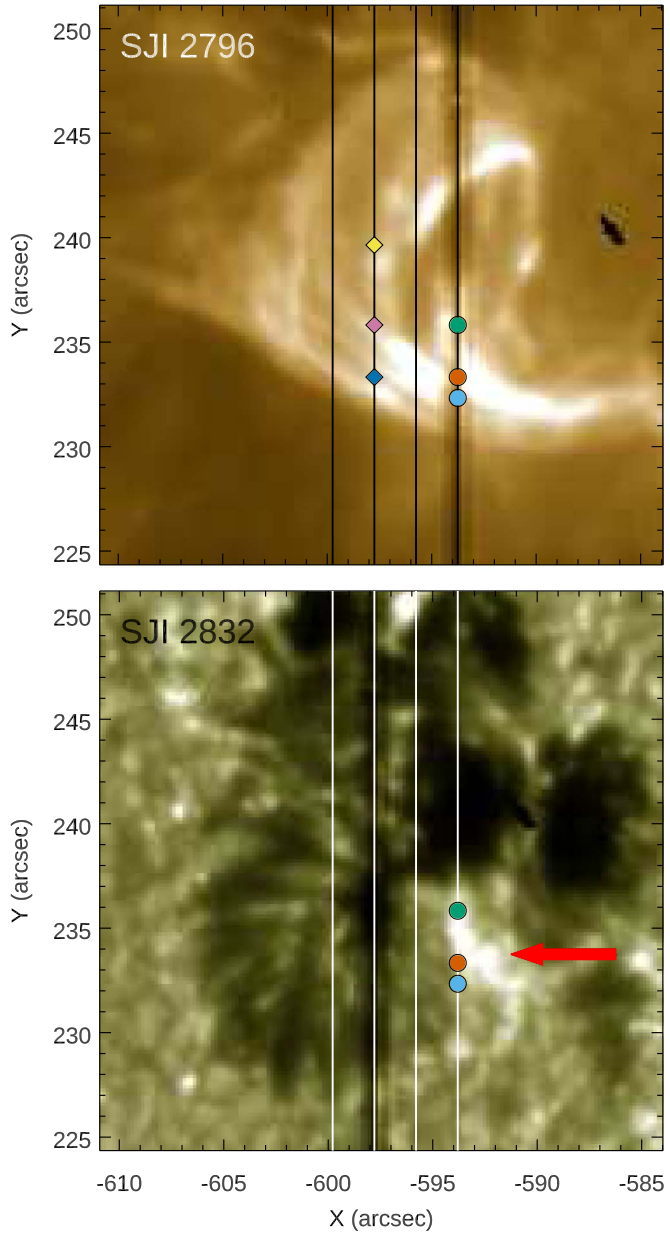

Figure 7. Zoomed maps at around 16:56 UT showing the details of δ-spot A, characterized by the presence of sheared penumbral filaments within the two opposite magnetic polarities. The sub-FOV is indicated with a dashed-line box in Figure 5. The blue, orange, and green circles indicate the slit positions used to determine the line profiles shown in Figures 8 and 9. Analogously, the colored diamonds indicate the slit positions of the profiles shown in Figure 10. The arrow indicates the brightening.

a double peak at 16:55:32 UT and becomes saturated at 16:56:47 and 16:57:24 UT. The blue pixel has profiles whose behavior is quite similar to that of the orange profile. However, in the former, there is a sudden increase of the upflows (up to $-100\,\mathrm{km\,s^{-1}}$) at 16:56:09 UT. At 16:57:24 UT, downflows of $\approx 25\,\mathrm{km\,s^{-1}}$ are detected.

If we examine the profiles reported in Figure 9 (second panels), relative to the C II 1335.75 Å line, we can infer a similar behavior to what we found in the Si IV 1402.8 Å line. In fact, the profiles relative to the green pixel exhibit downflows with velocities ranging between 60 and $100\,\mathrm{km\,s^{-1}}$; moreover, the line is saturated at 16:55:32 and 16:56:09 UT. The orange pixel shows a sudden change from upflows ($-50\,\mathrm{km\,s^{-1}}$) to downflows (up to $100\,\mathrm{km\,s^{-1}}$), similarly to the Si IV 1402.8 Å line. In this case, the line is saturated at 16:56:09 UT. The blue profile is akin to the orange profile, except for the sudden increase of the upflow, up to $-100\,\mathrm{km\,s^{-1}}$, observed at 16:56:09 UT.

Finally, the profiles of the Mg II h&k lines (shown in the bottom panels of Figure 9) indicate that during the analyzed time interval at the green position, there is evidence of downflows with velocities ranging between 35 and $40\,\mathrm{km\,s^{-1}}$ at the beginning; later on, these motions are no longer evident. The orange profiles are initially characterized by an upflow ($-65\,\mathrm{km\,s^{-1}}$), which later disappears. The behavior of the blue profiles is rather similar to that found in the orange profiles, but at this position, a sudden increase of the upflows (up to $-100\,\mathrm{km\,s^{-1}}$) occurs at 16:56:09 UT.

In Figure 10, we analyze the flux rope ejected at the beginning of the X1.6 flare. The slit sequentially crosses expanding sections of the ejected flux rope. This is clearly shown as the emitting area across the slit in the spectrograms widens with time.

Using a similar approach to that in Figure 9, we investigate the behavior of the UV emission in some pixel positions relative to the expanding flux rope in Figure 10. We indicate the approximate position of these pixels in Figure 7 (top panel) with colored diamonds. In particular, the slit position (1; 544) indicated by the blue diamond corresponds to the [−597.″8, 233.″3] solar coordinates at 16:56:47 UT, the position (1; 560) to [−597.″8, 235.″8] (magenta diamond), and the position (1; 582) to [−597.″8, 239.″6] (yellow diamond). We see that the yellow and magenta pixels exhibit upflows of about $-50\,\mathrm{km\,s^{-1}}$ since 16:54:54 UT. At the beginning, lines at chromospheric heights (C II and Mg II h&k) are stronger with respect to the background than the Si IV line. At the position indicated by the blue diamond, we see the intensity increase of the line profiles, indicating that the flux rope reaches that slit position and hotter plasma is observed. At 16:55:51 UT, we see a blue asymmetry in chromospheric lines. Interestingly, at 16:56:28 UT, we observe strong blue bumps with a blueshift of $\approx -60\,\mathrm{km\,s^{-1}}$ in the Si IV and C II lines. In the latter, we notice a blend with an absorption line, located at $\Delta\lambda \approx -80\,\mathrm{km\,s^{-1}}$, as well as a gap near the line center that moves from a blueshifted position at $Y \approx 580$ to a redshifted position at increasing Y values, until $Y \approx 620$. A similar behavior is observed at 16:57:06 UT, with a change from $\Delta\lambda \approx -40\,\mathrm{km\,s^{-1}}$ to $\Delta\lambda \approx +20\,\mathrm{km\,s^{-1}}$. At this time, we see different plasma components in the Si IV and C II lines, with one component characterized by upflows up to $-80\,\mathrm{km\,s^{-1}}$ and the other by moderate downflows of a few tens of $\mathrm{km\,s^{-1}}$. However, in all the lines, the blue pixel exhibits downward motions of about $+20\,\mathrm{km\,s^{-1}}$ at 16:57:06 UT. In the bulk of the chromosphere (Mg II h&k), at both 16:56:28 UT and 16:57:06 UT we find some locations with blueshifted mustaches in the spectroheliograms.

Unfortunately, the *IRIS* observations stop at this point, thus we cannot longer follow the expansion of the flux rope.

3.3. Changes in the Penumbrae

Figure 11 shows AR 12205 at the beginning of the X1.6 flare, as observed by *Hinode*/SOT in the G band. We indicate with a solid box the sub-FOV relative to the flaring δ-complex A observed to the northeast of AR 12205. The sequence of *Hinode*/SOT filtergrams displayed in Figure 12 manifests the concurrence of stable penumbral decay and enhancement in this area during the evolution of the observed flares. In

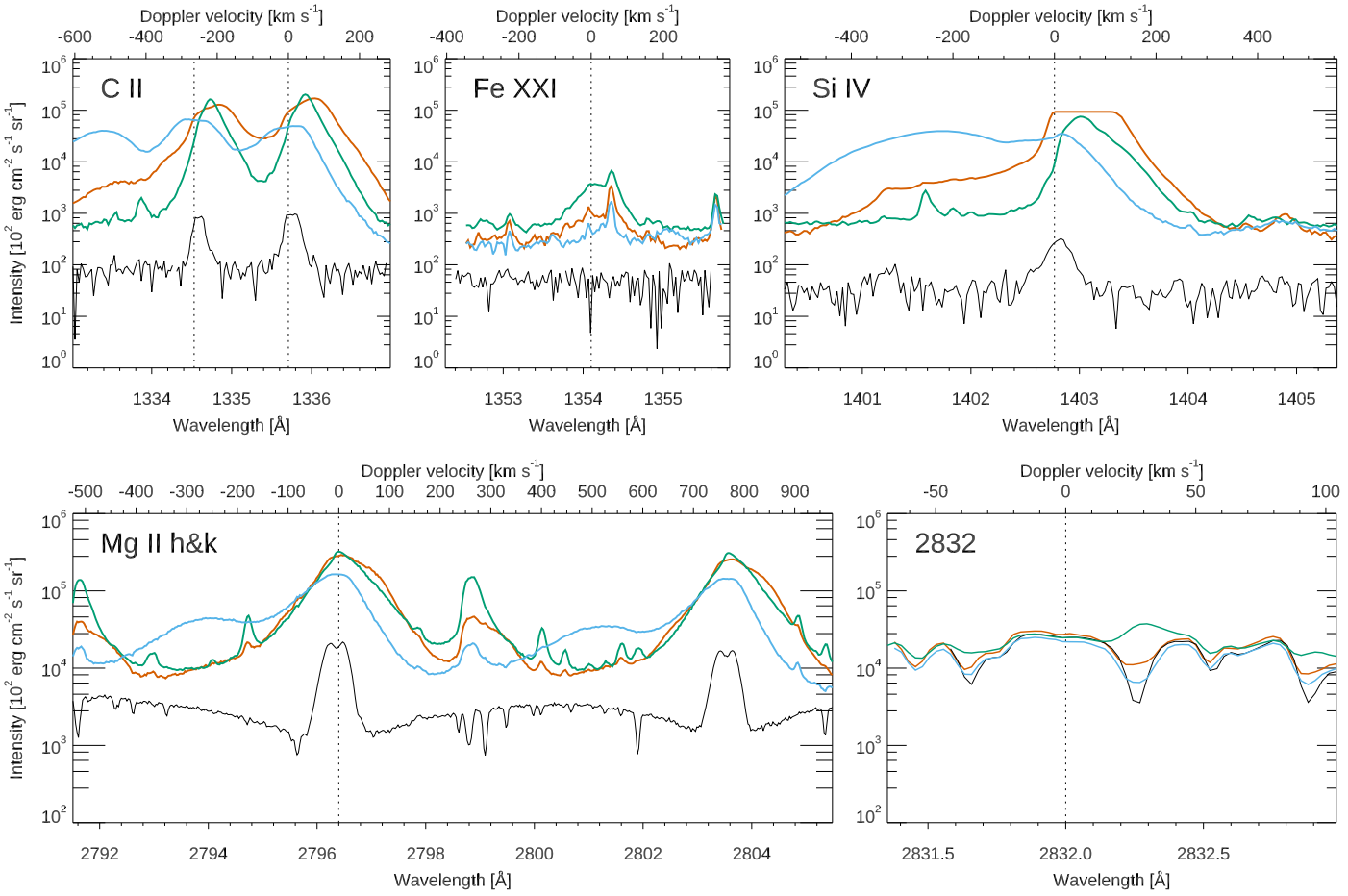

Figure 8. Average intensity as a function of wavelength in five of the IRIS spectral windows in the pixels at raster positions (3,[537:539]; blue), (3,[543:545]; orange), and (3,[558:560]; green) at 16:56:47 UT, corresponding to (−593″.8, 232″.3), (−593″.8, 233″.3), and (−593″.8, 235″.8), respectively. Black line: the average intensity calculated at the same time along the 20 consecutive slit positions (from 160 to 179), corresponding to a quiet-Sun region.

particular, after the X1.6 flare, the penumbra surrounding the eastern part of the negative spot of δ-complex A is intensely reduced, whereas penumbral filaments are enhanced along the polarity inversion line to the north of the same δ-complex and, above all, to the north of the protospot in the southwestern part of the sub-FOV of these filtergrams. The difference image between the first and last filtergrams in the sequence (Figure 12, bottom-right panel) clearly shows the areas of permanent penumbral decay (black) and enhancement (white). Note that we apply a mask, so that the black/white areas refer to regions where the normalized continuum intensities changed more than ± 0.15, in absolute value.

Using *SDO*/HMI SHARPs data with 12 minute cadence (Bobra et al. 2014), we were also able to obtain information about the magnetic field configuration in the region around δ-complex A, where penumbral decay/enhancements occur.

Figure 13 shows the same sub-FOV as Figure 12. The first two panels display the continuum maps from *SDO*/HMI before (15:11 UT) and after (18:47 UT) the C7.0 and X1.6 flares, where one can easily recognize the areas where penumbrae have disappeared or have newly formed. The remaining panels of Figure 13 are the difference images for the horizontal field component (third panel), vertical field component (fourth panel), and total magnetic field strength (fifth panel). The difference images were calculated with the sub-FOV of the magnetic field maps simultaneous with the continuum maps at 15:11 UT and 18:47 UT, respectively, as initial and final images. In these panels, we can see that major variations occur in the horizontal field component, which increases in the areas with penumbral enhancement (ΔB up to 1000 G) and, conversely, decreases in areas where penumbrae decay. This behavior is reflected in the variations of the total magnetic field strength as well. The changes in the vertical field component are smoother, except for a small area around the polarity inversion line of the δ-complex, where a strong variation larger than 1000 G occurs, also leading to a change in the magnetic polarity of the area.

The graph displayed in Figure 14 (top panel) illustrates that all the variations observed in the FOV corresponding to the difference images for the magnetic field component occur while the magnetic flux is almost constant. Only a slight decrease takes place between the two flares. On the other hand, if we focus our attention on a smaller FOV, indicated by the orange rectangle in Figure 13 (first panel), relative to the region occupied by the δ-complex, we notice that the positive magnetic flux (magenta circles) decreases during the selected time interval, while the negative flux (blue circles) shows an increase (Figure 14, middle panel). This behavior is even more evident if we consider the relative magnetic flux (see Figure 14, bottom panel). Nevertheless, the total magnetic flux remains almost constant, with a modest decrease after around 17:00. At that time, which corresponds to the onset of the X1.6 flare, the

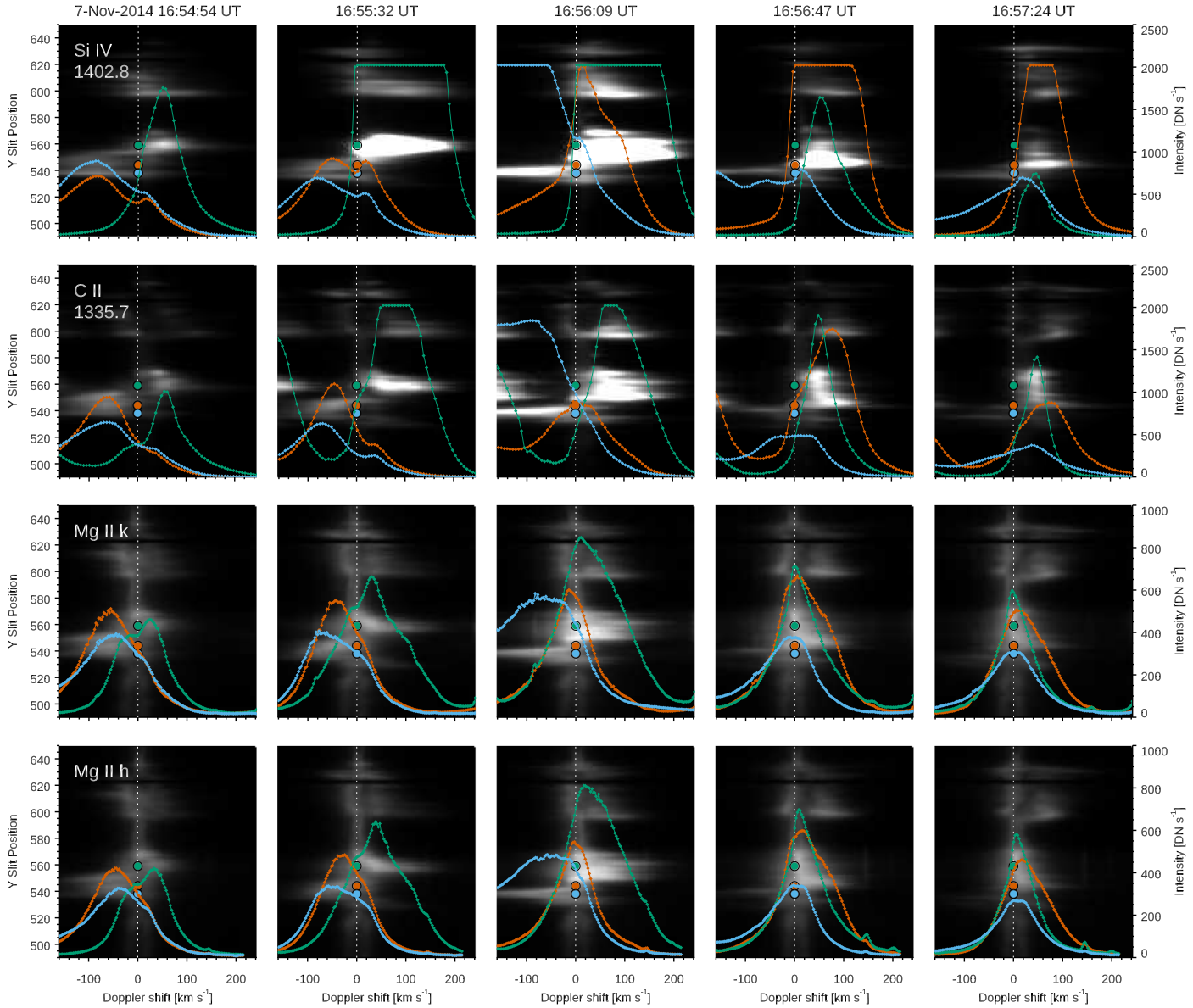

Figure 9. Line profiles for three different pixel positions of the *IRIS* slit for Si IV 1402.8 Å (top row), C II 1335.75 Å (second row), Mg II k 2796.31 Å (third row), and Mg II h 2803.55 Å (bottom row). In each row, the line profiles for successive times are overplotted on the relevant spectrograms. The dashed vertical lines indicate the position of the line center, while the blue, orange, and green circles show the slit positions relative to the profiles indicated with the same colors.

increase of the negative flux and the decrease of the positive flux begin.

4. Discussion

In this section, we discuss the main results obtained from the study of the consecutive C7.0 [SOL2014-11-07T16:10] and X1.6 [SOL2014-11-07T16:53] flares that occurred in AR 12205 on 2014 November 7, focusing on the following aspects: (1) flare triggering, (2) emission in the continuum and line profiles, and (3) changes in the penumbrae. We shall also demonstrate how these three aspects can be linked.

4.1. Flare Triggering

Small-scale energy releases, known as precursors, are often observed as preflare brightenings before the onset of large flares (Wang et al. 2017). In the case of AR 12205, a series of minor flares occurred on 2014 November 7 before the X1.6 flare [SOL2014-11-07T16:53]. Indeed, Sobotka et al. (2016) observed at high resolution the occurrence of some brightenings during the C3.9 flare with peak at 12:03 UT in δ-complex *B*, which hosted the circular ribbon of the flare. In addition, they saw signatures of slipping reconnection appearing as flare-like brightenings that first occurred in δ-complex *A* and then occurred southward and reached δ-complex *B*, where the C3.9 flare took place. Similarly, during the C7.0 flare that we analyzed [SOL2014-11-07T16:10], δ-complex *A* was first involved, with indication of a filament motion, and δ-complex *B* successively hosted the circular ribbon of the flare. Also during this event flare-like brightenings moved southward from δ-complex *A* to δ-complex *B* (see Figure 4, 16:25 UT).

The X1.6 flare was analyzed by Yurchyshyn et al. (2015), who reported that this flare began as a localized eruption of

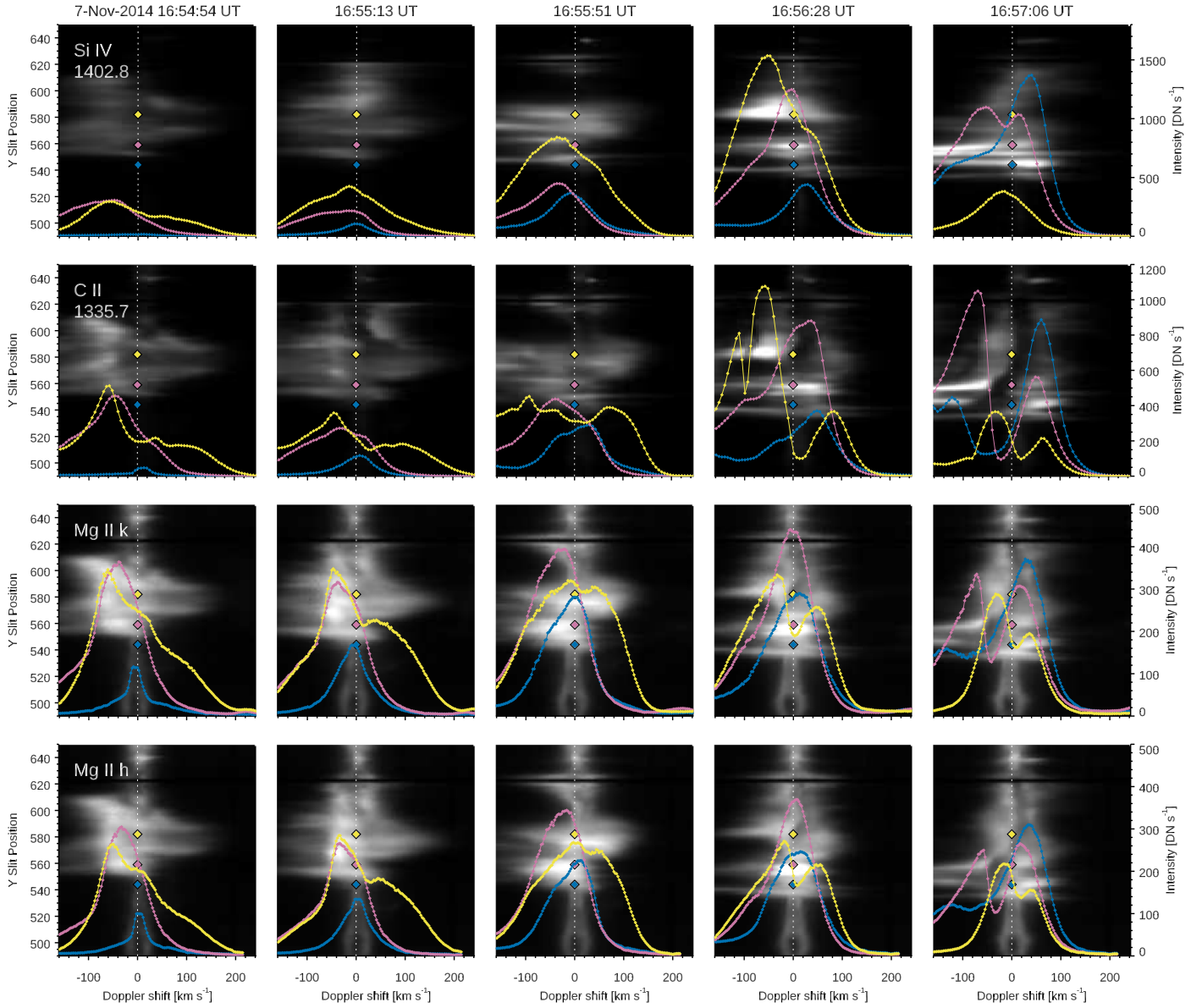

Figure 10. Same as in Figure 9, for the slit positions indicated with the blue, magenta, and yellow diamonds in Figure 7.

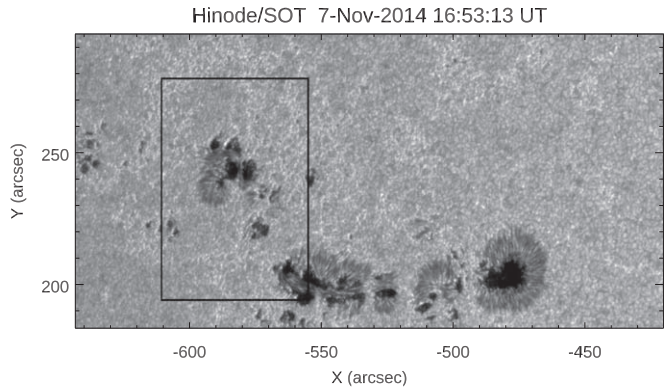

Figure 11. Map of the *G*-band intensity taken by *Hinode*/SOT at the beginning of the X1.6 flare. The box frames the sub-FOV used in Figure 12, relative to δ-complex *A*.

core fields inside the northern δ-complex *A*, triggered by flux emergence occurring at the boundary between the two umbrae. Later, the event involved the entire AR, releasing a fast and wide coronal mass ejection (CME). They found that this event was accompanied by posteruption arcades, J-shaped flare ribbons exhibiting fine structures, and irreversible changes in the magnetic configuration in the photosphere.

According to Yurchyshyn et al. (2015), the X1.6 flare and the related filament eruption were triggered by magnetic flux emergence at the boundary between the two umbrae of opposite polarity of δ-complex *A*. To support this claim, they rely on the analysis of the magnetic flux trend within these umbrae using HMI measurements (see Figure 1 in Yurchyshyn et al. 2015). However, while the authors indicate that they employed HMI data from the hmi.B_720s series, which of course have a cadence of 12 minutes, in the plot the cadence appears to be different.

Our measurements of the total magnetic flux in that area disagree with those reported by Yurchyshyn et al. (2015): the total magnetic flux in the area remains almost constant, and instead shows a slight decrement (Figure 14). There is only an increase of the negative magnetic flux, which is roughly compensated by the decrease of the positive magnetic flux.

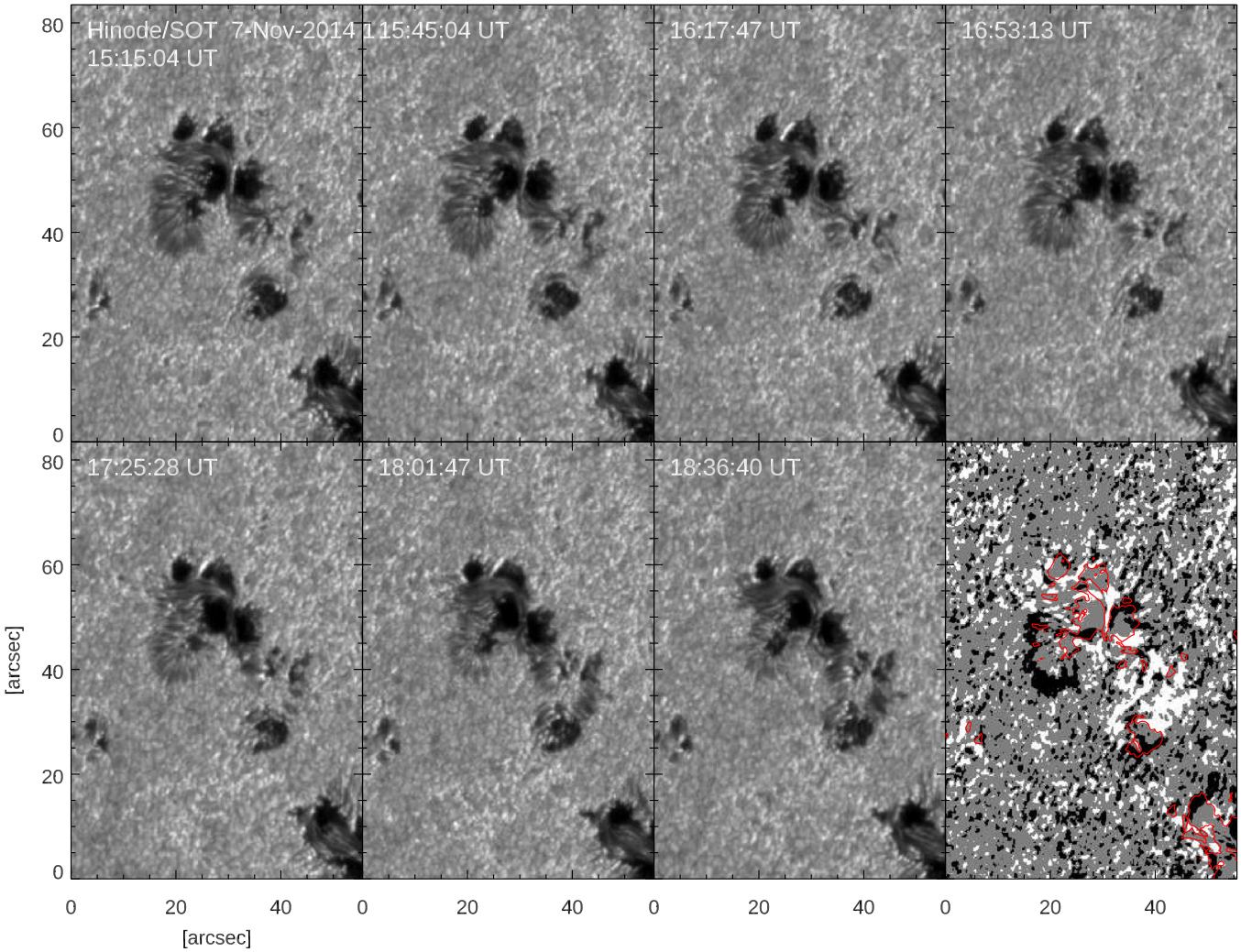

Figure 12. Panels 1–7: photospheric evolution of δ-complex *A* during the C7.0 and X1.6 flares, as seen by *Hinode*/SOT in *G* band. Bottom-right panel: difference image between the first and last *G*-band filtergrams of the *Hinode*/SOT sequence. White (black) areas indicate regions with penumbral enhancement (decay). Red contours indicate the umbral boundary at the beginning of the sequence.

Indeed, Figure 13 clearly shows that in the interface region between the two opposite-polarity umbral cores of δ-complex *A*, the magnetic field changes sign (fourth panel). In addition, there is a variation of distribution of the total field strength toward the north of δ-complex *A*: the magnetic field strengthens in the left area and decreases in the right area, mainly due to an analog variation in the strength of the horizontal field.

Therefore, from our analysis, it appears that flux emergence cannot be invoked as the trigger mechanism of these flares. In contrast, combining our findings with the analysis carried out by Yurchyshyn et al. (2015), it can be deduced that the eruption of a flux rope occurred in δ-complex *A* region, where the presence of strongly sheared field lines was witnessed by penumbral filaments aligned along the PIL between the two opposite umbral cores (see Figure 5 in Yurchyshyn et al. 2015). After the C7.0 and X1.6 flares, penumbral filaments reached a more relaxed configuration, as demonstrated by the azimuth changes detected by Yurchyshyn et al. (2015). The increasing energy content of the flares that occurred before the onset of the X1.6 flare, together with the precursor brightenings, the shaking motion of the filament connecting δ-complexes *A* and *B* seen during the C7.0 flare, and its sigmoidal configuration along the PIL, just before the X1.6 flare, suggest that AR 12205 was progressively destabilized. In this perspective, the eruption of the flux rope observed at the beginning of the X1.6 flare seems to have triggered a kind of domino effect (see, e.g., Zuccarello et al. 2009), which eventually caused the launching of the filament that settled along the PIL that later formed the CME observed by LASCO.

4.2. Emission in the Continuum and Line Profiles

During the rise phase of the X1.6 flare (at 16:57 UT), signatures of emission in the continuum close to the wings of the Mg II k line were detected (*IRIS* data set), while a few minutes before the flare peak, a ribbon was observed in the *G* band and in the 4170 Å continuum (ROSA data set). The areas of enhanced emission involved δ sunspots in the northern and southern parts of AR 12205. In particular, around the peak time of the X1.6 class flare, the ROSA data set shows the presence of bright ribbons at continuum wavelengths separating at an average velocity of $\approx$10 km s^{-1}.

Concerning the physical processes at work, it has been suggested that hydrogen recombination in the chromosphere might have an important role in flare WL emission. More

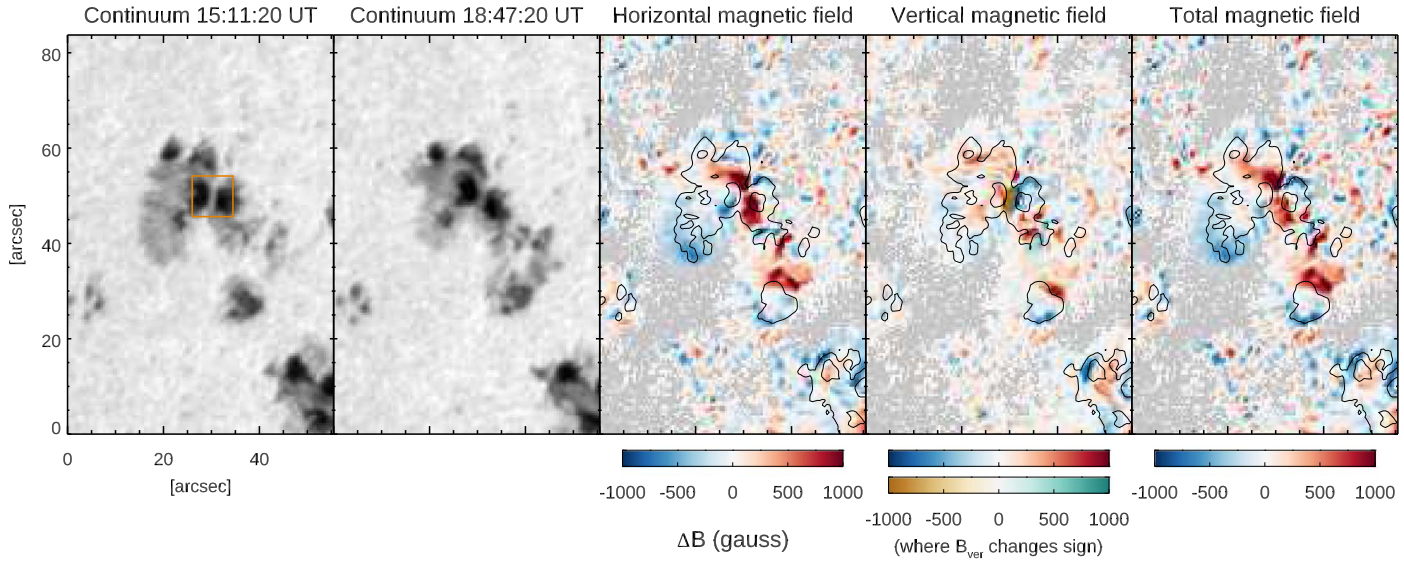

Figure 13. First and second panels: continuum images relative to the same sub-FOV as used for the analysis of the *Hinode*/SOT filtergrams (see Figure 12), for *SDO*/HMI before (15:11 UT) and after (18:47 UT) the flares. Third, fourth, and fifth panels: difference images between the final and initial maps of the horizontal field component, vertical field component, and total magnetic field strength. The gray background indicates pixels with total magnetic field strength < 100 G, not considered. The color bars represent the variation of the magnetic field components and of the total field strength (blue: -1000 G; red: 1000 G). The extra color bar indicates the variation of the vertical component of the magnetic field where it changes sign (yellow: -1000 G; green: 1000 G).

specifically, the hydrogen recombination occurring in the chromosphere may be related to the so-called radiative backwarming, so that there is an increase of temperature in the photosphere that can produce the optically thick flare emission in the continuum (Hudson 1972; Metcalf et al. 1990a, 1990b; Ding & Fang 1996).

With regard to UV line profiles, it is generally believed that the transport of energy from the coronal reconnection site to the chromosphere implies the occurrence of a beam of accelerated (nonthermal) electrons that impact the chromosphere and cause chromospheric evaporation. Observations indicate the presence of chromospheric heating such that hot (8–25 MK) upflows (up to -400 km s^{-1}) along the flare loops are detected in SXR and EUV. The heated plasma expands upward at the sound speed, while at the same time, the chromospheric plasma is strongly compressed and downward-propagating shock waves are excited in the chromosphere.

During the impulsive phase of flares, some authors observed redshifts and enhancements in the red wing of chromospheric lines (Tei et al. 2018 and references therein). In Hα, downward plasma velocities of $\sim$50 km s^{-1} have been measured and have been interpreted in terms of momentum balance with upflows of the chromospheric plasma (Ichimoto & Kurokawa 1984).

Švestka et al. (1962) analyzed the line asymmetries in the spectra of 92 flares and found evidence that 80% of them showed red asymmetry and 23% show blue asymmetry. Later, Heinzel et al. (1994) found that the Balmer and the Ca II H lines show blue asymmetry during the onset phase of flares.

Kerr et al. (2015) using Mg II *IRIS* data found redshifts equivalent to velocities of 15–26 km s^{-1}, while Graham & Cauzzi (2015) found upflows of up to 300 km s^{-1} and downflows up to 40 km s^{-1} during the impulsive phase.

Tei et al. (2018) analyzed a C-class flare using data in the Si IV 1403 Å, C II 1335 Å, and Mg II h&k lines from *IRIS* and the Ca II K, Ca II 8542 Å, and Hα lines from the Domeless Solar Telescope. They found that in the Mg II h line, the leading edge of the flare kernel showed an intensity enhancement in the blue wing, and a smaller intensity of the blue-side peak than that of the red side. The blueshift lasted for 9–48 s with a typical speed of 10.1 ± 2.6 km s^{-1}, and it was followed by the high intensity and large redshift with a speed of up to 50 km s^{-1} detected in the Mg II h line. The large redshift was a common property for all six lines but the blueshift prior to it was found only in the Mg II lines. Similarly, studying Mg II lines during an M6.5 flare, Huang et al. (2019) observed blue-wing enhancement, with typical blueshifts of about 10 km s^{-1}, up to 20 km s^{-1}, and strong broadening on the leading edge of the propagating ribbon, while redshifts were observed in the trailing areas. Comparing their observations with numerical modeling, Huang et al. (2019) suggested that the enhanced blue wings in Mg II lines can be due to an increase of local electron density and a decrease in temperature, caused by electron precipitation, whereas a spatially unresolved turbulence of 10–30 km s^{-1} can be responsible for the broadening.

The analysis carried out in this work shows that for Si IV (see Figure 9, top panel), the line profiles and velocity values for the pixel positions indicated by the orange and blue circles in Figure 7 indicate upflows followed by downflows, while the line profile at the position denoted by the green circle is indicative of downflows in the analyzed time interval.

If we interpret these upflows and downflows in the framework of processes of evaporation and condensation associated with the standard flare model, we can conclude that in two of the three pixels examined, a process of chromospheric evaporation is followed by condensation, while in the third slit position there is continuous condensation.

In the framework of the same scenario, for C II (see Figure 9, second panel) in two among the three pixel positions examined, a process of chromospheric evaporation is followed by a condensation (orange and blue profiles), while in the third slit position there is continuous condensation (green profiles).

In the case of Mg II k&h (see Figure 9, third and fourth panels), the line profiles and the velocity values for the pixel positions indicated by the orange and blue circles in Figure 7 demonstrate the presence of upflows between 16:54 and 16:56 UT, while the line profile at the position indicated by the green circle suggests downflows. Different pixel positions indicate

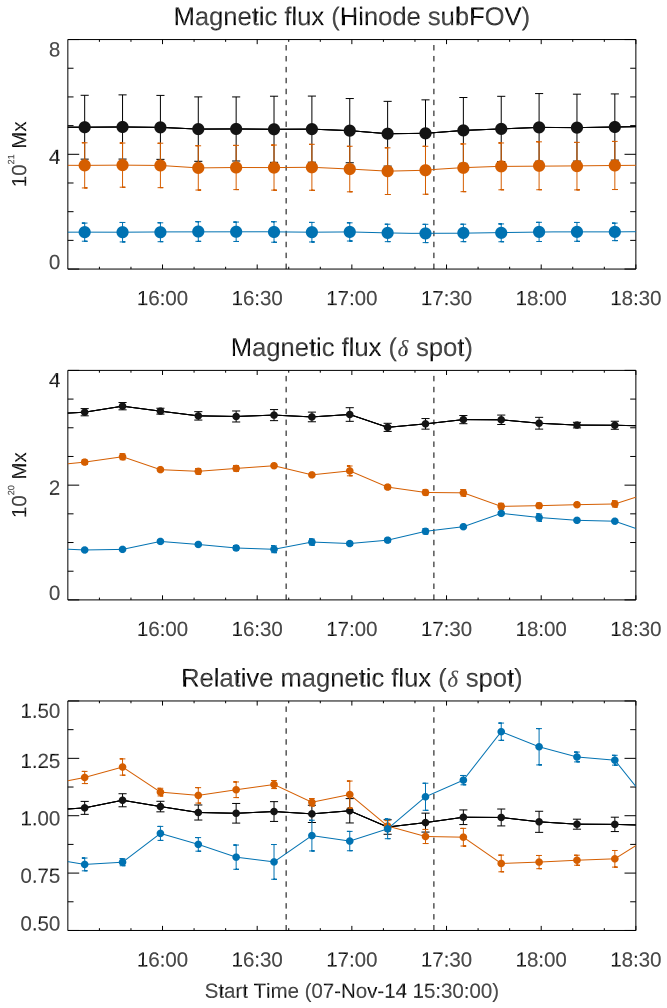

Figure 14. Top panel: the total unsigned magnetic flux (black), positive flux (orange), and negative flux (blue, in absolute value), relative to the *Hinode* sub-FOV around δ-spot *A* shown in Figure 13. Middle panel: same, for the sub-FOV relative to the inner part of the δ-spot, indicated with a box in the first panel of Figure 13. Bottom panel: the relative change of the total unsigned magnetic flux (black), positive flux (orange), and negative flux (blue, in absolute value), with respect to the average values, the sub-FOV relative to the inner part of the δ-spot. The peak time of the C7.0 (16:39 UT) and X1.6 (17:26 UT) flares are indicated by vertical dashed lines. Error bars represent 1σ value.

that at the same time, process of chromospheric evaporation and condensation are taking place.

In summary, in this scenario, for selected time intervals and slit positions at the flare ribbon, the line profiles of C II 1335.75 Å, Si IV 1402.8 Å, and Mg II k&h may suggest the occurrence of a process of chromospheric evaporation followed by condensation taking place at different atmospheric heights, given different formation temperatures of the lines. The rising flux rope may explain an electron influx to the ribbon, causing evaporation as well as providing a source for the continuum enhancements.

An alternative explanation for the presence of blueshifts at some slit positions could be related with the upward motion of the erupting filament at the beginning of the X1.6 flare. Recently, Kleint et al. (2015) found Doppler shifts ranging between -100 to $-600\,\mathrm{km\,s^{-1}}$ in *IRIS* Si IV spectra during the filament eruption leading to an X1 flare. Typical velocities of eruptions of filaments are of the same order of magnitude, ranging from less than $100\,\mathrm{km\,s^{-1}}$ up to $1000\,\mathrm{km\,s^{-1}}$, even if they depend on the height of the measurements (see Kleint et al. 2015 and references therein).

The upward velocities inferred in our study from the analysis of different lines range between -50 and $-100\,\mathrm{km\,s^{-1}}$; therefore, we cannot completely discard the hypothesis that these blueshifts might be related to the motions of the rising filament. However, our analysis of *IRIS* data relevant to the flux rope shows a rather different pattern in the spectroheliograms and in the individual line profiles, the upward velocities of the erupting filament being in general slightly larger than those observed in the ribbon.

On the other hand, an enhancement of continuum emission in FUV and NUV, as well as a very prominent bump in the blue wing of the Si IV, C II, and Mg II h&k lines were detected (see Figure 8). Based on the previous considerations, we propose that this bump cannot be attributed to the upward velocity component of the ejected flux rope, because the line profiles in this structure do not exhibit such a broadened line. Indeed, the *IRIS* slit caught the structure during the launch phase, as shown in Figure 6. The bump is more prominent higher in the atmosphere (Si IV) than at chromospheric heights (Mg II h&k lines). This could suggest that we see the effect of reconnection due to magnetic braiding, as in the launch of jets (see, e.g., Huang et al. 2018), resulting in a large, nonthermal broadening of the lines.

4.3. Changes in the Penumbrae

With regard to the observed changes in the penumbrae around the sunspots involved in the C7.0 and X1.6 flares, our analysis highlights that these are due to magnetic fields in the regions around sunspots becoming more vertical or horizontal, leading to the decay or enhancement of penumbral regions, respectively. This finding confirms the suggestion by Liu et al. (2005) about the flare-associated changes in WL continuum intensity being related to permanent variations in the inclination as a result of the reconnection in δ-sunspots. It also supports the close correlation between the changes in the sunspot intensity and horizontal field strength which was studied by Song & Zhang (2016) in a sample of flaring ARs, including AR 12205 after the X1.6 flare.

Recent observations of the magnetic field rearrangement in the photosphere after an M5.0 solar flare show that the inner penumbral enhancement around the flaring PIL area was accompanied by the field collapsing down, whereas the outer penumbral decay area was associated with the field lifting up toward the upper flare center (Xu et al. 2019). In contrast, 3D simulations suggest that observed enhancement in the photospheric horizontal magnetic fields along the PIL results from the reconnection-driven contraction of sheared flare loops, which increases the downward component of the Lorentz force density around the PIL (Barczynski et al. 2019).

AR 12205 was also included in the sample of ARs investigated by Lu et al. (2019) to evaluate the magnetic imprints of X-class flares in the photosphere, in the context of backreaction on the solar surface associated with coronal field restructuring (Hudson et al. 2008; Wang & Liu 2010). In this study, the X1.6 flare of AR 12205 was considered an event that increased the horizontal field component only along the PIL (Lu et al. 2019).

In our observations, we also found evidence for penumbral formation (see the region at around [40″, 40″] in panel 8, Figure 12). Yurchyshyn et al. (2015) observed that these

penumbral-like features, similar to orphan penumbrae (e.g., Lim et al. 2013), were developed under a stable filament, and they were not related to the presence of opposite-polarity fields around a PIL. We suggest that the overlying filament is trapping part of the magnetic flux whose orientation has been modified by the flare into a more horizontal configuration. This is supported by the fact that we did not observe any variation of the magnetic flux in the *Hinode* sub-FOV around δ-complex *A* (see Figure 14, top panel); therefore, it appears that the formation of these penumbral-like structures is not linked to flux emergence. Indeed, invoking such a mechanism able to lead to the presence of highly inclined, nearly horizontal magnetic fields being responsible for penumbra formation (or, conversely, decay) strengthens the argument which has been proposed in recent studies concerning the development of penumbrae and penumbral-like structures, from both the observational (see, e.g., Shimizu et al. 2012; Lim et al. 2013; Romano et al. 2013, 2014; Guglielmino et al. 2014, 2017, 2019; Jurčák et al. 2014, 2017; Zuccarello et al. 2014; Murabito et al. 2016, 2017, 2018) and the theoretical points of view (Rempel 2012; MacTaggart et al. 2016), even in the absence of magnetic flux variations. In this perspective, our findings indicate that the effects of magnetic reconfiguration leading to penumbral enhancements driven by flares can extend well beyond the region around the flaring PILs.

In connection with backreaction analysis, our findings relative to δ-complex *A* are in agreement with the qualitative observational signature proposed by Wang & Liu (2010): the observed limbward flux increases while diskward flux decreases rapidly and irreversibly after the C7.0 and X1.6 flares. This can be easily noticed in the difference image between the final and initial maps of the vertical field component (Figure 13, panel four) and in the graph of the relative magnetic flux in Figure 14 (bottom panel).

5. Conclusions

We studied two consecutive C7.0 and X1.6 flares occurred in AR 12205 using data acquired by ground-based and satellite instruments. Our analysis brought new information to interpret these events, which showed a complex behavior.

Both the *IRIS* and the ROSA data sets show the presence of bright ribbons at continuum wavelengths around the peak time of the X1.6 class flare. The WL emission, if interpreted in the framework of hydrogen recombination in the chromosphere, may be related to radiative backwarming, due to an increase in the temperature at the photospheric level.

The interpretation of the line profiles of C II 1335.75 Å, Si IV 1402.8 Å, and Mg II k&h has been discussed in two scenarios. The former, based on the hypothesis of the occurrence of plasma motions foreseen in the standard flare model, seems to suggest the occurrence of a process of chromospheric evaporation followed by condensation, which takes place at different atmospheric heights, as seen in lines with different formation temperatures. The latter scenario, which seems to be the most plausible, taking into account both the line profiles and the presence of a very prominent bump in the blue wing of Si IV, C II, and Mg II h&k, is based on the hypothesis that the blueshifts detected at some slit positions are actually indicative of the rising motion of an eruptive filament.

As far as the flare's triggering mechanism is concerned, comparing our analysis with the one carried out by Yurchyshyn et al. (2015), we can conclude that the eruption of a flux rope triggered these events, so that the release of the shear stored in the field lines, rather than flux emergence, is the main reason for the flare occurrence.

In this scenario, tether-cutting reconnection could be considered a plausible mechanism for the formation of the unstable flux rope (Moore et al. 2001; Yurchyshyn et al. 2006; Chen et al. 2016; Xue et al. 2017). Such a mechanism is often invoked to explain the backreaction on the solar surface that we have noticed in our observations as well (e.g., Wang & Liu 2010; Lu et al. 2019). On the other hand, slipping reconnection seems to be at work during these events, as witnessed by the appearance of the bright elongated patch observed to the east of the δ-spot region a few minutes after the onset of the X1.6 flare. Indeed, such a configuration with a third, remote brightening site is reminiscent of a fan-spine topology, with the dome-shaped fan located above δ-complex *A* (see, e.g., Guglielmino et al. 2016). This seems to be confirmed by the analysis of the previous C7.0 flare.

Finally, concerning the changes in the penumbrae observed during the flares, our analysis provided indications that the overlying filament can trap part of the magnetic flux system that has been modified by the flare, becoming more horizontal, and that the magnetic reconfiguration can also take place in a region far from the PIL.

We believe that the next generation of ground-based telescopes, like the European Solar Telescope (Collados et al. 2010) and the Daniel K. Inouye Solar Telescope (Keil et al. 2010) will be fundamental to shed light on some of the issues that remain to be further investigated and clarified. These issues include (but are not limited to) the possibility to impute, and to what degree, how flare triggering is related to magnetic flux emergence and/or shearing and how to distinguish the motion associated with an erupting filament with processes associated with plasma evaporation/condensation. Another key process that remains to be addressed is the relationship between continuum enhancement and magnetic field rearrangement.

The authors wish to thank the anonymous referee for helpful comments. The research leading to these results has received funding from the European Commissions Seventh Framework Programme under grant agreement Nos. 606862 (F-CHROMA project) and 312495 (SOLARNET project), and from the European Union's Horizon 2020 research and innovation programme under grant agreement Nos. 739500 (PRE-EST project) and 824135 (SOLARNET project). This work was supported by the Italian MIUR-PRIN grant 2012P2HRCR on "The active Sun and its effects on space and Earth climate," by the Space Weather Italian COmmunity (SWICO) Research Program, and by the Università degli Studi di Catania (Piano per la Ricerca Università di Catania 2016-2018—Linea di intervento 1 "Chance"; Linea di intervento 2 "Ricerca di Ateneo—Piano per la Ricerca 2016/2018"). P.H.K. is grateful to the Leverhulme Trust for the award of an Early Career Fellowship. *IRIS* is a NASA small explorer mission developed and operated by LMSAL with mission operations executed at NASA Ames Research center and major contributions to downlink communications funded by ESA and the Norwegian Space Centre. The *SDO*/HMI data used in this paper are courtesy of NASA/*SDO* and the HMI science team. *Hinode* is a Japanese mission developed and launched by ISAS/JAXA, with NAOJ as domestic partner and NASA and STFC (UK) as international partners. It is operated by these agencies in

cooperation with ESA and Norwegian Space Centre. Use of NASA's Astrophysical Data System is gratefully acknowledged.

Facilities: Hinode (SOT), *IRIS*, *SDO* (HMI, AIA).

ORCID iDs

Francesca Zuccarello https://orcid.org/0000-0003-1853-2550
Salvo L. Guglielmino https://orcid.org/0000-0002-1837-2262
Mihalis Mathioudakis https://orcid.org/0000-0002-7725-6296
Peter H. Keys https://orcid.org/0000-0001-8556-470X
Serena Criscuoli https://orcid.org/0000-0002-4525-9038
Mariarita Murabito https://orcid.org/0000-0002-0144-2252

References

Aschwanden, M. J. 2004, Physics of the Solar Corona (Chichester: Praxis Publishing Ltd.)
Aulanier, G., Démoulin, P., Schrijver, C. J., et al. 2013, A&A, 549, A66
Aulanier, G., Golub, L., DeLuca, E. E., et al. 2007, Sci, 318, 1588
Aulanier, G., Janvier, M., & Schmieder, B. 2012, A&A, 543, A110
Aulanier, G., Pariat, E., Démoulin, P., & DeVore, C. R. 2006, SoPh, 238, 347
Barczynski, K., Aulanier, G., Masson, S., et al. 2019, ApJ, 877, 67
Benz, A. O. 2017, LRSP, 14, 2
Bobra, M. G., Sun, X., Hoeksema, J. T., et al. 2014, SoPh, 289, 3549
Carmichael, H. 1964, in Proc. AAS-NASA Symp.—The Physics of Solar Flares, ed. W. N. Hess (Washington: National Aeronautics and Space Administration, Science and Technical Information Division), 451
Castellanos Durán, J. S., Kleint, L., & Calvo-Mozo, B. 2018, ApJ, 852, 25
Chen, H., Zhang, J., Li, L., & Ma, S. 2016, ApJL, 818, L27
Collados, M., Bettonvil, F., Cavaller, L., & Team, E. S. T. 2010, AN, 331, 615
Cristaldi, A., Guglielmino, S. L., Zuccarello, F., et al. 2014, ApJ, 789, 162
De Pontieu, B., Title, A. M., Lemen, J. R., et al. 2014, SoPh, 289, 2733
Démoulin, P. 2006, AdSpR, 37, 1269
Ding, M. D., & Fang, C. 1996, A&A, 314, 643
Dudík, J., Janvier, M., Aulanier, G., et al. 2014, ApJ, 784, 144
Dudík, J., Polito, V., Janvier, M., et al. 2016, ApJ, 823, 41
Fletcher, L., Dennis, B. R., Hudson, H. S., et al. 2011, SSRv, 159, 19
Fletcher, L., & Hudson, H. S. 2008, ApJ, 675, 1645
Graham, D. R., & Cauzzi, G. 2015, ApJL, 807, L22
Guglieilmino, S. L., Romano, P., Ruiz Cobo, B., Zuccarello, F., & Murabito, M. 2019, ApJ, 880, 34
Guglielmino, S. L., Romano, P., & Zuccarello, F. 2017, ApJL, 846, L16
Guglielmino, S. L., Zuccarello, F., Romano, P., et al. 2014, ApJL, 786, L22
Guglielmino, S. L., Zuccarello, F., Romano, P., et al. 2016, ApJ, 819, 157
Heinzel, P., Karlicky, M., Kotrc, P., & Svestka, Z. 1994, SoPh, 152, 393
Hirayama, T. 1974, SoPh, 34, 323
Hoeksema, J. T., Liu, Y., Hayashi, K., et al. 2014, SoPh, 289, 3483
Huang, N., Xu, Y., Sadykov, V. M., et al. 2019, ApJL, 878, L15
Huang, Z., Xia, L., Nelson, C. J., et al. 2018, ApJ, 854, 80
Hudson, H. S. 1972, SoPh, 24, 414
Hudson, H. S., Acton, L. W., Hirayama, T., & Uchida, Y. 1992, PASJ, 44, L77
Hudson, H. S., Fisher, G. H., & Welsch, B. T. 2008, in ASP Conf. Ser. 383, Subsurface and Atmospheric Influences on Solar Activity, ed. R. Howe et al. (San Francisco, CA: ASP), 221
Ichimoto, K., & Kurokawa, H. 1984, SoPh, 93, 105
Janvier, M. 2017, JPlPh, 83, 535830101
Janvier, M., Aulanier, G., Pariat, E., & Démoulin, P. 2013, A&A, 555, A77
Jess, D. B., Mathioudakis, M., Christian, D. J., et al. 2010, SoPh, 261, 363
Jess, D. B., Mathioudakis, M., Crockett, P. J., & Keenan, F. P. 2008, ApJL, 688, 119
Jurčák, J., Bello González, N., Schlichenmaier, R., & Rezaei, R. 2014, PASJ, 66, S3
Jurčák, J., Bello González, N., Schlichenmaier, R., & Rezaei, R. 2017, A&A, 597, A60
Keil, S. L., Rimmele, T. R., Wagner, J., & Team, A. T. S. T. 2010, AN, 331, 609
Kerr, G. S., Simões, P. J. A., Qiu, J., & Fletcher, L. 2015, A&A, 582, A50
Kleint, L., Battaglia, M., Reardon, K., et al. 2015, ApJ, 806, 9
Kopp, R. A., & Pneuman, G. W. 1976, SoPh, 50, 85
Kosugi, T., Matsuzaki, K., Sakao, T., et al. 2007, SoPh, 243, 3
Lemen, J. R., Title, A. M., Akin, D. J., et al. 2012, SoPh, 275, 17
Lim, E.-K., Yurchyshyn, V., Goode, P., & Cho, K.-S. 2013, ApJL, 769, L18
Liu, C., Deng, N., Liu, Y., et al. 2005, ApJ, 622, 722
Lu, Z., Cao, W., Jin, G., et al. 2019, ApJ, 876, 133
Machado, M. E., Emslie, A. G., & Avrett, E. H. 1989, SoPh, 124, 303
MacTaggart, D., Guglielmino, S. L., & Zuccarello, F. 2016, ApJL, 831, L4
Masson, S., Pariat, E., Aulanier, G., & Schrijver, C. J. 2009, ApJ, 700, 559
Maurya, R. A., & Ambastha, A. 2009, SoPh, 258, 31
Metcalf, T. R., Canfield, R. C., Avrett, E. H., & Metcalf, F. T. 1990a, ApJ, 350, 463
Metcalf, T. R., Canfield, R. C., & Saba, J. L. R. 1990b, ApJ, 365, 391
Milligan, R. O. 2015, SoPh, 290, 3399
Moore, R. L., Sterling, A. C., Hudson, H. S., et al. 2001, ApJ, 552, 833
Murabito, M., Romano, P., Guglielmino, S. L., & Zuccarello, F. 2017, ApJ, 834, 76
Murabito, M., Romano, P., Guglielmino, S. L., Zuccarello, F., & Solanki, S. K. 2016, ApJ, 825, 75
Murabito, M., Zuccarello, F., Guglielmino, S. L., & Romano, P. 2018, ApJ, 855, 58
Neidig, D. F. 1989, SoPh, 121, 261
Neidig, D. F., & Cliver, E. W. 1983, SoPh, 88, 275
Patsourakos, S., Georgoulis, M. K., Vourlidas, A., et al. 2016, ApJ, 817, 14
Pesnell, W. D., Thompson, B. J., & Chamberlin, P. C. 2012, SoPh, 275, 3
Petrie, G. J. D. 2012, ApJ, 759, 50
Petrie, G. J. D. 2013, SoPh, 287, 415
Petrie, G. J. D., & Sudol, J. J. 2010, ApJ, 724, 1218
Piersanti, M., Alberti, T., Bemporad, A., et al. 2017, SoPh, 292, 169
Rempel, M. 2012, ApJ, 750, 62
Rimmele, T. R. 2004, ApJ, 604, 906
Romano, P., Falco, M., Guglielmino, S. L., & Murabito, M. 2017, ApJ, 837, 173
Romano, P., Frasca, D., Guglielmino, S. L., et al. 2013, ApJL, 771, L3
Romano, P., Guglielmino, S. L., Cristaldi, A., et al. 2014, ApJ, 784, 10
Scherrer, P. H., Schou, J., Bush, R. I., et al. 2012, SoPh, 275, 207
Shimizu, T., Ichimoto, K., & Suematsu, Y. 2012, ApJL, 747, L18
Sobotka, M., Dudík, J., Denker, C., et al. 2016, A&A, 596, A1
Song, Y. L., & Zhang, M. 2016, ApJ, 826, 173
Sturrock, P. A. 1966, Natur, 211, 695
Švestka, Z., Kopecký, M., & Blaha, M. 1962, BAICz, 13, 37
Tei, A., Sakaue, T., Okamoto, T. J., et al. 2018, PASJ, 70, 100
Toriumi, S., & Wang, H. 2019, LRSP, 16, 3
Tsuneta, S., Ichimoto, K., Katsukawa, Y., et al. 2008, SoPh, 249, 167
Wang, H., & Liu, C. 2010, ApJL, 716, L195
Wang, H., & Liu, C. 2015, RAA, 15, 145
Wang, H., Liu, C., Ahn, K., et al. 2017, NatAs, 1, 0085
Wang, S., Liu, C., Deng, N., & Wang, H. 2014, ApJL, 782, L31
Wang, S., Liu, C., Liu, R., et al. 2012a, ApJL, 745, L17
Wang, S., Liu, C., & Wang, H. 2012b, ApJL, 757, L5
Wöger, F., von der Lühe, O., & Reardon, K. 2008, A&A, 488, 375
Xu, Z., Yang, J., Ji, K., Bi, Y., & Yang, B. 2019, ApJ, 874, 134
Xue, Z., Yan, X., Yang, L., Wang, J., & Zhao, L. 2017, ApJL, 840, L23
Yurchyshyn, V., Karlický, M., Hu, Q., & Wang, H. 2006, SoPh, 235, 147
Yurchyshyn, V., Kumar, P., Cho, K.-S., Lim, E.-K., & Abramenko, V. I. 2015, ApJ, 812, 172
Zheng, R., Chen, Y., & Wang, B. 2016, ApJ, 823, 136
Zuccarello, F., Balmaceda, L., Cessateur, G., et al. 2013, JSWSC, 3, A18
Zuccarello, F., Guglielmino, S. L., & Romano, P. 2014, ApJ, 787, 57
Zuccarello, F., Romano, P., Farnik, F., et al. 2009, A&A, 493, 629